

Global simulation of tropospheric O₃-NO_x-hydrocarbon chemistry

2. Model evaluation and global ozone budget

Yuhang Wang,¹ Jennifer A. Logan, and Daniel J. Jacob

Department of Earth and Planetary Sciences and Division of Engineering and Applied Sciences, Harvard University, Cambridge, MA 02138

Abstract. Results from a global three-dimensional model for tropospheric O₃-NO_x-hydrocarbon chemistry are presented and evaluated with surface, ozonesonde, and aircraft measurements. Seasonal variations and regional distributions of ozone, NO, peroxyacetyl nitrate (PAN), CO, ethane, acetone, and H₂O₂ are examined. The model reproduces observed NO and PAN concentrations to within a factor of 2 for a wide range of tropospheric regions including the upper troposphere but tends to overestimate HNO₃ concentrations in the remote troposphere (sometimes several fold). This discrepancy implies a missing sink for HNO₃ that does not lead to rapid recycling of NO_x; only in the upper troposphere over the tropical South Atlantic would a fast conversion of HNO₃ to NO_x improve the model simulation for NO_x. Observed concentrations of acetone are reproduced in the model by including a large biogenic source (15 Tg C yr⁻¹), which accounts for 40% of the estimated global source of acetone (37 Tg C yr⁻¹). Concentrations of H₂O₂ in various regions of the troposphere are simulated usually to within a factor of 2, providing a test for HO_x chemistry in the model. The model reproduces well the observed concentrations and seasonal variations of ozone in the troposphere, with some exceptions including an underestimate of the vertical gradient across the tropical trade wind inversion. A global budget analysis in the model indicates that the supply and loss of tropospheric ozone are dominated by photochemistry within the troposphere and that NO_x emitted in the southern hemisphere is twice as efficient at producing ozone as NO_x emitted in the northern hemisphere.

1. Introduction

In a companion paper [Wang *et al.*, this issue(a)], we described the formulation of a global three-dimensional model for the simulation of tropospheric O₃-NO_x-hydrocarbon chemistry. We present here an evaluation of model results for ozone, reactive nitrogen oxides, CO, ethane, acetone, and H₂O₂ with observations in different regions of the troposphere. This extensive evaluation provides the basis for using the model to investigate global and regional budgets of tropospheric ozone in a second companion paper [Wang *et al.*, this issue(b)]. It also provides important constraints on our understanding of tropospheric ozone chemistry.

The model is driven by meteorological fields from a general circulation model (GCM) developed at the Goddard Institute for Space Studies [Hansen *et al.*, 1983]. It has a spatial resolution of 4° latitude by 5° longitude, with seven vertical layers extending from the surface to 150 mbar. Meteorological fields are updated every 4 hours. Spatially and temporally varying cross-tropopause fluxes of ozone, NO_x, and HNO₃ are specified as upper boundary conditions at 150 mbar. The model transports 15 tracers including odd oxygen ($O_x = O_3 + O + NO_2 + HNO_4 + 2 \times NO_3 + 3 \times N_2O_5$), NO_x ($NO + NO_2 + NO_3 + HNO_2$), N₂O₅, HNO₃, HNO₄, peroxyacetyl nitrates, alkyl ni-

trates, CO, ethane, ($\geq C_4$) alkanes, ($\geq C_3$) alkenes, isoprene, acetone, ($\geq C_4$) ketones, and H_2O_2 . Detailed representation of tropospheric O_3 - NO_x -hydrocarbon chemistry and process-based representations of emission and deposition are included [Wang *et al.*, this issue(a)].

The GCM is intended to simulate a typical meteorological year, not any particular year of the observations; our evaluation of model results focuses therefore on observed seasonal statistics. Multiyear observations needed to produce robust seasonal statistics are available only for ozone [Logan, 1985; Oltmans and Levy, 1994; J. A. Logan, An analysis of ozonesonde data, 1, Its application in testing models of tropospheric chemistry, manuscript in preparation, 1998 (hereinafter referred to as Logan, manuscript in preparation, 1998)] and surface CO [Novelli *et al.*, 1992, 1994]; even with these data, site coverage is mostly in the northern midlatitudes as shown in Figure 1 for ozone. Atmospheric observations of CH_3CCl_3 offer a valuable constraint for the evaluation of the global mean OH in the model [Prinn *et al.*, 1995]. For other species simulated in the model including NO, peroxyacetylnitrate (PAN), HNO_3 , C_2H_6 , acetone, and H_2O_2 , aircraft campaigns provide the main source of observations. We make use of data from the NASA Global Tropospheric Experiment and other aircraft expeditions [Bradshaw *et al.*, 1998, and references therein]. Compiled aircraft observations with a resolution of 1° latitude \times 1° longitude \times 1-km altitude [Bradshaw *et al.*, 1998] were obtained from Scott Smyth of the Georgia Institute of Technology. Since aircraft data are limited in their temporal and spatial coverage, we aggregate them over the regions as shown in Figure 2. We do not use aircraft observations of NO_2 and total reactive nitrogen oxides (NO_y) for model evaluation, as these measurements are of questionable quality [Crosley, 1996; Bradshaw *et al.*, 1998].

We present our evaluation of model results with observations starting from the global mean OH (section 2), followed by reactive nitrogen oxides (section 3), CO (section 4), ethane (section 5), acetone (section 6), H_2O_2 (section 7), and ozone (section 8). An analysis of the global budget of tropospheric ozone is presented in section 9, and conclusions are in section 10.

2. Global Mean OH

Figure 3 shows the zonal mean OH concentrations simulated by the model for January and July. The latitudinal and seasonal variations reflect to a large extent the distributions of UV radiation and water vapor which provide the primary source of OH through the reaction $O(^1D) + H_2O$ [Levy, 1971]. Summertime concentrations are higher in the northern hemisphere than in the southern hemisphere owing to the role of anthropogenic ozone and NO_x in enhancing OH production; this enhancement more than compensates for the depletion of OH caused by anthropogenic CO and hydrocarbons [Thompson, 1992].

The global mean OH concentration simulated in the model is evaluated using measurements of CH_3CCl_3 , a gas emitted by

Figure 1

Figure 2

Figure 3

industry and removed principally by OH oxidation [Prinn *et al.*, 1987]. Based on observed atmospheric concentrations of CH_3CCl_3 and industrial emission inventories, Prinn *et al.* [1995] derived a lifetime of 4.9 ± 0.3 years for CH_3CCl_3 below 200 mbar against oxidation by OH. In comparison, we obtain in our model a lifetime of 5.1 years for CH_3CCl_3 below 200 mbar against oxidation by OH. Our simulated global mean OH concentration in the troposphere below 200 mbar is 1.0×10^6 molecules cm^{-3} weighted by atmospheric mass and 1.2×10^6 molecules cm^{-3} weighted by the temperature-dependent loss rate of CH_3CCl_3 . Prinn *et al.* [1995] reported a value of $0.97 \pm 0.03 \times 10^6$ molecules cm^{-3} for the latter quantity, assuming an effective temperature of 277 K for the computation of the CH_3CCl_3 loss rate. However, a more appropriate choice for the effective temperature is 262 K [Prather and Spivakovsky, 1990], which yields a mean OH concentration of 1.3×10^6 molecules cm^{-3} , similar to the value reported here.

3. Reactive Nitrogen Oxides

3.1. Nitric Oxide

Simulated NO_x concentrations near the surface and at 500 mbar are shown in Figure 4 for January and July. Concentrations over the eastern United States in summer are in the range of 1-2 parts per billion by volume (ppbv), consistent with observations compiled by Horowitz *et al.* [1998]. The rapid decrease of NO_x concentrations away from continental source regions reflects the oxidation of NO_x to HNO_3 on a timescale of a day in the lower troposphere. Globally, about half of this oxidation takes place by the reaction of NO_2 with OH and half by the hydrolysis of N_2O_5 in aerosols, similar to the previous model results of Dentener and Crutzen [1993]. NO_x concentrations at 500 mbar in the northern hemisphere are lower in winter than in summer, reflecting decreased production by lightning and decreased convective export from polluted continents. Thermal decomposition of PAN is an important source for NO_x in the remote lower atmosphere in the model [Jacob *et al.*, 1992; Fan *et al.*, 1994; Moxim *et al.*, 1996].

Emmons *et al.* [1997] presented a comparison of our simulated NO_x concentrations at 0- to 6- km altitude with ground-based and aircraft observations. They found no significant anomalies. We choose to focus our comparison on observations for NO, which are considered more reliable than observations of NO_x [Crosley, 1996; Crawford *et al.*, 1996]. Figure 5 shows observed and simulated vertical profiles of daytime NO for the 24 regions of Figure 2; model results are averages for the months of observations. The model reproduces closely the concentrations observed in the extratropical northern hemisphere, where fossil fuel combustion is the dominant source of NO_x ; the overestimate of NO off the coast of Japan (region 14) in October is due to a strong influence of Asian outflow to the region in the model, as will be shown more clearly in the comparison for PAN. The observed decrease of NO concentrations away from the continental source regions is well simulated. A

Figure 4

Figure 5

trend toward higher NO concentrations is found in the upper troposphere in both model and observations, owing principally in the model to increases in the NO/NO₂ concentration ratio and in the lifetime of NO_x.

The model simulates well the particularly low NO concentrations observed over the tropical Pacific (regions 16, 17, 23). Higher NO concentrations in the upper troposphere over New Guinea (region 24) are due to the source from lightning, which we scaled globally to 3 Tg N yr⁻¹ to match the aircraft observations over the northern equatorial Atlantic [Drummond *et al.*, 1988; Smyth *et al.*, 1996], a region remote from fossil fuel and biomass burning influence. Over Amazonia (regions 7, 8), soil emissions are thought to be the main source for the observed NO_x concentrations in the boundary layer [Jacob and Wofsy, 1988, 1990]. These emissions are higher in the dry season (August) than in the wet season (May) [Bakwin *et al.*, 1990], resulting in higher NO concentrations in the dry season in both the observations and the model. The overestimate at 500 mbar over Amazonia reflects in the model a large (and perhaps excessive) lightning source of NO in the region.

Measurements during the Transport and Atmospheric Chemistry Near the Equator – Atlantic (TRACE-A) Expedition in September-October 1992 [Fishman *et al.*, 1996] show a large enhancement of NO concentrations over the tropical South Atlantic and neighboring continents owing to emissions from biomass burning. The model captures well these enhancements below 400 mbar but is somewhat lower in the upper troposphere (regions 9-13). A possible reason for this discrepancy is proposed below in light of comparisons of model results with HNO₃ observations.

3.2. Nitric Acid

Simulated HNO₃ concentrations near the surface and at 500 mbar are shown in Figure 6 for January and July. Nitric acid is produced mainly by the reaction of NO₂ with OH and by hydrolysis of N₂O₅ in aerosols and is removed by wet and dry deposition. To some extent, the distribution of HNO₃ mimics that of NO_x (Figure 4). The mean lifetime of HNO₃ against wet deposition in the model ranges from 5 days in the boundary layer to 2-3 weeks in the upper troposphere [Balkanski *et al.*, 1993]. In the boundary layer the lifetime of HNO₃ against dry deposition is between a few hours and few days depending on surface type, mixed layer depth, and season.

Model results for HNO₃ in the eastern United States in summer are consistent with mean observed values of 1-1.5 ppbv at rural sites [Parrish *et al.*, 1993]. In the remote troposphere, by contrast, model values are often several times larger than those observed (Figure 7). Fractionation of HNO₃ into the aerosol phase may provide a partial explanation. The model does not resolve gas phase HNO₃(g) from aerosol nitrate (NO₃⁻), while the observations are for HNO₃(g) only. Observations available from aircraft in the remote troposphere indicate NO₃⁻/HNO₃(g) molar ratios of 0.3 to 1, increasing from northern midlatitudes to the tropics [Singh *et al.*, 1996]; the eastern United States data of Parrish *et al.* [1993] indicate lower ratios

Figure 6

Figure 7

in the range of 0.1-0.4. Another possible reason for the excessive HNO_3 in the model may be that scavenging from convective precipitation is underestimated, because the wet convective transport scheme does not allow for entrainment [Koch *et al.*, 1996]. Still, the combined effect of these factors does not appear enough to fully explain the discrepancy.

Previous authors have noted that observed HNO_3 concentrations in the remote troposphere are several times lower than would be expected from gas phase chemical steady state with NO and proposed rapid conversion of HNO_3 to NO_x in aerosols to explain this discrepancy [Chatfield, 1994; Fan *et al.*, 1994; Hauglustaine *et al.*, 1996; Jacob *et al.*, 1996]. However, our model simulates well observed NO concentrations in most regions (Figure 5), where HNO_3 is overestimated; introducing an additional mechanism for recycling HNO_3 to NO_x to match observed HNO_3 would result in large overestimates of NO particularly in the lower and middle troposphere. One exception is the upper troposphere over the tropical South Atlantic (regions 11,12) where simulated NO concentrations are lower than observations from the TRACE-A aircraft campaign, while simulated HNO_3 concentrations are higher.

To investigate this issue further, we conducted a sensitivity simulation that includes an arbitrary conversion of HNO_3 to NO_x above 400 mbar with a first-order rate constant $k = 0.3 \text{ day}^{-1}$ [Jacob *et al.*, 1996]. Figure 8 shows the resulting distributions of upper tropospheric NO and HNO_3 over the tropical South Atlantic (TRACE-A) and over the western tropical and subtropical Pacific (Pacific Exploratory Mission (PEM) West-A) as a function of longitude and latitude, respectively. We find that addition of the HNO_3 recycling reaction improves the simulations of both NO_x and HNO_3 in the TRACE-A region. Concentrations of NO are increased by a factor of 2, matching observations better; the longitudinal gradient across the Atlantic is suppressed, in agreement with observations. Increasing the primary sources of NO_x from lightning or biomass burning to accommodate the TRACE-A observations would fail to reduce the longitudinal gradient across the tropical Atlantic, since these sources are continental. For the PEM West-A region, by contrast, rapid recycling HNO_3 to NO_x in the model leads to an overestimate of NO by about a factor of 2. Our model analysis thus provides support for rapid recycling of HNO_3 to NO_x in limited regions of the upper troposphere (as in TRACE-A) but also suggests that this recycling is not ubiquitous.

3.3. Peroxyacetylnitrate

Peroxyacetylnitrate is formed by the reaction of NO_2 with peroxyacetyl radicals originated from the oxidation of non-methane hydrocarbons (NMHCs). Its main sink in the lower and middle troposphere is by thermolysis, the rate of which decreases rapidly with decreasing temperature [Atkinson *et al.*, 1992]. Additional loss by photolysis takes place in the upper troposphere [Talukdar *et al.*, 1995]. In the analysis that follows, we assume that PAN is the main component of the lumped peroxyacetylnitrate tracer in the model. Figure 9 shows

Figure 8

Figure 9

simulated PAN concentrations near the surface and at 500 mbar for January and July. Concentrations of PAN are generally higher in the northern hemisphere than in the southern hemisphere owing to NO_x emissions from fossil fuel combustion. Model results for the eastern United States in summer are consistent with observations at rural sites (0.5-1.5 ppbv) [Parish *et al.*, 1993]. High concentrations of PAN are also simulated over the biomass burning regions of the tropical continents. Except over continental source regions, concentrations of PAN are generally higher at 500 mbar than in surface air because of lower temperatures and hence longer lifetimes for PAN.

Comparison of observed and simulated vertical profiles for PAN is shown in Figure 10. The concentrations of PAN are well simulated over Alaska in summer (region 1) but are overestimated over Canada (regions 2, 3). This discrepancy appears to be related to excessive transport of polluted air from the eastern United States to Canada in the model, a problem previously identified in a simulation of sulfate [Chin *et al.*, 1996].

Model results for northern midlatitudes (the United States, the Pacific, and eastern Asia) (regions 4, 5, 14, 15, 19, 20) are generally consistent with observations, although the variability in the observations is large. PAN concentrations off the coast of Japan (region 14) are overestimated by at least a factor of 2 in October, suggesting that the export of PAN from the Asian continent to the region is too strong in the model, as was previously indicated by the comparison for NO (Figure 5).

Concentrations of PAN in the tropics are usually very low, both in the model and observations (regions 16, 17, 23, 24). The model overestimates concentrations over Amazonia (regions 7, 8), reflecting the overestimate for NO discussed previously. The TRACE-A observations over Brazil (regions 9, 10), southern Africa (regions 12, 13), and the tropical South Atlantic (region 11) show enhanced PAN concentrations associated with biomass burning. The model simulation lies within the range of observations, although model values appear too low over eastern Brazil (region 9); the layers of elevated concentrations of PAN in the upper troposphere over the South Atlantic (region 11) and off the west coast of southern Africa (region 12) are not captured by the model.

4. Carbon Monoxide

Figure 11 shows the simulated CO concentrations near the surface and at 500 mbar for January and July. Higher concentrations in the northern hemisphere than in the southern hemisphere and over continents than over oceans reflect the distribution of combustion sources. The model matches well the observed atmospheric concentrations and seasonal variations of CO at most sites where multiyear records are available [Novelli *et al.*, 1992, 1994], except for an underestimate at high northern latitudes in winter (largest in Barrow, Alaska) and an overestimate (about 10 ppbv) at southern middle and high latitudes. Comparisons of model results with observations are shown in Figure 12 for eight representative sites. Detailed evaluation of a global simulation for CO in a similar model will be presented in a separate publication currently in prepa-

Figure 10

Figure 11

Figure 12

ration by J. A. Logan.

5. Ethane

Ethane is released by industrial and combustion sources and is removed by OH oxidation with a lifetime of a few months; concentrations are higher in the northern hemisphere than in the southern hemisphere and are higher in winter than in summer. Model results are compared in Figure 13 with observed vertical distributions, in Figure 14 with observed seasonal variations at four surface sites, and in Figure 15 with the total ethane column observed over Lauder, New Zealand [Rinsland *et al.*, 1994]. The model generally underestimates observations. The global ethane source of 8.8 Tg C yr^{-1} in our model [Wang *et al.*, this issue(a)] is lower than the estimates of 12-13 Tg C yr^{-1} derived by Kanakidou *et al.* [1991] and Rudolph [1995] to fit observed atmospheric ethane concentrations in their two-dimensional models. An independent emission inventory by Rudolph [1995] indicates a total source of $10.4 \text{ Tg C yr}^{-1}$ contributed mainly by natural gas leaks (4.8 Tg C yr^{-1}) and biomass burning (5.1 Tg C yr^{-1}). The industrial source of ethane in our model (6.3 Tg C yr^{-1}) is higher than that of Rudolph [1995], whereas our biomass burning source (2.5 Tg C yr^{-1}) is lower. Biogenic sources of ethane appear to be small [Rudolph, 1995].

Over Alaska (region 1), our underestimate of ethane may be explained by emissions from local oil drilling and Siberian coal fields not included in the model [Blake *et al.*, 1992]. At northern midlatitudes the model tends to overestimate ethane concentrations at continental surface sites while underpredicting aircraft measurements; the reasons are unclear. Simulated monthly mean C_2H_6 columns for Kit Peak (30°N , 122°W) agree well with the long-term measurement by C. P. Rinsland (personal communication, 1998).

Model results for the southern hemisphere capture the observed springtime maximum in ethane concentrations, which is due in the model to biomass burning; however, simulated concentrations tend to be much lower than those observed in all seasons. Increasing the biomass burning source in the model from 2.5 Tg C yr^{-1} to 6 Tg C yr^{-1} would improve the model simulations (Figures 14 and 15). This increase would require doubling either the biomass burning source for CO or the ethane/CO emission ratio, neither of which seems likely on the basis of model evaluation for CO (Figure 11) and measured ethane/CO emission ratios from fires [Wang *et al.*, this issue(a)]. There is little variability in measured ethane/CO emission ratios from different fires because both gases are emitted at the smoldering stage of a fire [Lobert *et al.*, 1991]. The sensitivity simulation of a larger biomass burning source suggests an underestimate of ethane emissions for the southern hemisphere in the model; however, the available measurements in the southern hemisphere do not appear to provide further constraints on the origin of this underestimate.

6. Acetone

Sources of acetone in the model include 1 Tg C yr^{-1} from

Figure 13

Figure 14

Figure 15

industry, 9 Tg C yr⁻¹ from biomass burning, 15 Tg C yr⁻¹ from the terrestrial biosphere, and 12 Tg C yr⁻¹ from the oxidation of propane and higher alkanes [Wang *et al.*, this issue(a)]. The source of acetone from the terrestrial biosphere may include both direct emission and secondary production from biogenic hydrocarbons [Singh *et al.*, 1994]; we assume this source to have the same spatial distribution as isoprene and adjust its magnitude to match the few observed vertical profiles of acetone concentrations in the tropics [Wang *et al.*, this issue(a)]. The production of acetone from propane oxidation is treated as a primary source scaled to the propane emission inventory and assuming an 80% yield of acetone; this procedure was adopted to avoid having to include propane as a tracer in the model. The production from oxidation of higher alkanes by contrast is computed within the model as a secondary source. Loss of acetone is by photolysis [McKeen *et al.*, 1997] and oxidation by OH. Calculated lifetimes for acetone in the tropics are 1-2 months in the lower troposphere and 2-3 weeks in the upper troposphere. The global mean lifetime of acetone in the model is 26 days.

Simulated acetone concentrations near the surface and 500 mbar are shown in Figure 16 for January and July. Concentrations are usually higher in winter than in summer owing to a longer lifetime, and are higher in the northern hemisphere than in the southern hemisphere owing to a large source from oxidation of industrial propane and higher alkanes.

Figure 17 shows the comparison of observed and simulated vertical profiles for acetone. Simulated concentrations over eastern Canada (region 3) are lower than observations by a factor of 2. Analysis of observations in this region indicates major sources from vegetation and biomass burning, with only about a 20% contribution from industrial activities [Singh *et al.*, 1994; Wofsy *et al.*, 1994]. The vegetation source at high northern latitudes may be underestimated in the model as a result of scaling to isoprene emissions, which are relatively low in that region. Observed acetone concentrations over the remote tropical Pacific are well simulated (regions 22, 23), reflecting the adjustment of the biogenic source in the model. The higher concentrations observed in the TRACE-A region (regions 10-13), also well simulated by the model, reflect the additional contribution from biomass burning emissions.

The model overestimates acetone concentrations in the Asian outflow over the subtropical western Pacific in February (regions 20, 21). This discrepancy appears to be caused by treating acetone production from propane oxidation as a primary source in the model. Since the lifetime of propane is over a week in winter, the model would overpredict acetone concentrations near source regions. The error is small in summer or in the tropics and is of little consequence for regions influenced primarily by biomass burning such as TRACE-A, where the primary source of acetone from biomass burning is much larger than the production from alkane oxidation [Wang *et al.*, this issue(a)].

Singh *et al.* [1995] previously presented a global three-dimensional simulation of acetone using the MOGUNTIA model [Kanakidou and Crutzen, 1993]. Although our global source of acetone is only 20% higher than theirs, the two models have large differences in simulated concentrations. The

Figure 16

Figure 17

zonal mean concentrations simulated by MOGUNTIA for the southern hemisphere (about 50 pptv) and for the upper troposphere (50-200 pptv at 200 mbar) are considerably lower than observations (Figure 17). Our model results in these regions (Figure 18) are about a factor of 3 higher than in MOGUNTIA and are in better agreement with observations. The cause of the discrepancy between the two models is unclear.

Figure 18

7. Hydrogen Peroxide

Simulated H_2O_2 concentrations near the surface and at 500 mbar are shown in Figure 19 for January and July. Hydrogen peroxide is produced by the self-reaction of HO_2 and is thus a sensitive proxy for HO_x radicals ($\text{HO}_x = \text{OH} + \text{HO}_2$). It is removed by reaction with OH, photolysis, and wet and dry deposition. Concentrations of H_2O_2 are higher in summer than in winter and are higher in the tropics than at high latitudes, reflecting the dependence of HO_x production on solar radiation and water vapor.

Figure 19

Figure 20 shows the comparison of observed and simulated vertical profiles for H_2O_2 . The model matches observations in the Asian outflow and over the tropical western Pacific but underestimates H_2O_2 below 500 mbar over the TRACE-A biomass burning regions (regions 9, 10, 12). Over eastern Brazil (region 9), boundary layer H_2O_2 concentrations at night are diluted in the model by inflow of low- H_2O_2 air from the Atlantic carried by easterly winds exceeding 10 m s^{-1} . Primary emission of H_2O_2 by fires [Lee *et al.*, 1997], not included in the model, may also contribute to the underestimate. It is not clear why observed concentrations of H_2O_2 over the southern coast of Brazil (region 10) are so high, considering that these specific observations were for relatively dry remote air which originated from southern midlatitudes [Browell *et al.*, 1996].

Figure 20

8. Ozone

8.1. Seasonal Variation

Simulated ozone concentrations near the surface and at 500 mbar are shown in Figure 21 for January and July. Elevated ozone concentrations are simulated over industrial regions of the northern hemisphere in summer and over the biomass burning regions of tropical continents, as observed [Logan, 1985; Andreae *et al.*, 1992; Helas *et al.*, 1995; Fishman *et al.*, 1996]. We compare in Figures 22a-22d the observed and simulated seasonal variations of ozone near the surface and at 800, 500, and 300 mbar, respectively. The observations at 800-300 mbar are from multiyear ozonesonde measurements (Logan, manuscript in preparation, 1998). Surface ozone observations are 24-hour averages, except for the sites over the continental United States, where the observations are for 1300-1600 local time. Jacob *et al.* [1993] pointed out that evaluation of model results with observations in continental surface air should focus on the afternoon hours, when observations are most likely to be representative of a deep mixed layer that can be resolved by the model. This constraint does not apply to marine sites where diel variability is small [Oltmans and Levy,

Figure 21

Figure 22a-22d

1994].

Observed ozone concentrations in the lower troposphere of the extratropical northern hemisphere are generally simulated to within 10 ppbv by the model. A major feature of the observations in this region is the summertime maximum at polluted sites and the springtime maximum at remote sites [Logan, 1985]. This feature is well simulated by the model; the origin of the springtime maximum is discussed by Wang *et al.* [this issue(b)]. The observed springtime minimum in surface air at Barrow, Alaska, is thought to be caused by bromine-catalyzed ozone depletion taking place in a shallow mixed layer [Barrie *et al.*, 1988; Oltmans and Levy, 1994], which is not accounted for in the model. The observed summertime minima of about 20 ppbv at Bermuda and at the Japanese island sites reflect the influence of long-range transport of tropical air with low ozone; this tropical influence is not represented properly in the GCM.

The seasonality of ozone in the tropical lower troposphere is well simulated by the model. However, the model overestimates ozone concentrations by up to 20 ppbv at some sites, owing to excessive subsidence from the free troposphere as discussed further in the next section. The summer minimum at Barbados reflects rapid photochemical loss [Oltmans and Levy, 1994]. The austral spring maxima at Natal and Cuiaba are due to biomass burning. Observed ozone concentrations at Brazzaville in austral spring are 40 ppbv higher at 800 mbar than in surface air, reflecting advection of relatively clean marine air below the trade wind inversion by a monsoon flow [Cros, 1987], which is not captured by the model.

Observed lower tropospheric ozone concentrations at middle and high latitudes of the southern hemisphere are reproduced by the model to within 10 ppbv. The observations show a winter maximum in surface air, reflecting the seasonality of photochemical loss, and a spring maximum at 800 mbar reflecting the long-range transport of biomass burning effluents [Fishman *et al.*, 1991]. The model shows a spring maximum at 800 mbar but also at the surface, which we explain as owing to excessive exchange between the boundary layer and the free troposphere at high southern latitudes.

Ozonesonde observations in the northern extratropics show a broad spring-summer maximum extending up to the tropopause [Logan, 1985; Logan, manuscript in preparation, 1998]. This seasonal pattern is captured by the model (Figures 22c and 22d). The model also reproduces well observed ozone concentrations in the northern extratropics at 500 mbar (Figure 22c). However, simulated ozone concentrations are too low at 300 mbar (Figure 22d), which is frequently in the stratosphere in the observations [Holton *et al.*, 1995; Logan, manuscript in preparation, 1998] but not in the model [Koch *et al.*, 1996]. We removed stratospheric data from the ozonesonde observations north of 35°N using the temperature measurements available for each sonde (Logan, manuscript in preparation, 1998). Figure 22d shows that model results are in close agreement with the filtered tropospheric data at 300 mbar.

Model results at 500 and 300 mbar are generally in good agreement with observations in the northern tropics but too low in the southern tropics. The 25-ppbv underestimate of ozone concentrations at Natal, Ascension, and Pretoria in aus-

tral spring is related in part to the underestimate of NO_x concentrations in the upper troposphere over the tropical South Atlantic, as was discussed in section 3.1, and in part to excessive vertical mixing in the model across the trade wind inversion, as will be discussed below. Including rapid HNO_3 recycling to NO_x in the upper troposphere as described in section 3.2 would increase ozone concentrations by 5-15 ppbv in the upper troposphere over the tropical South Atlantic, improving the agreement with observations.

8.2. Vertical Profiles

Simulated vertical profiles of ozone concentrations in different seasons are compared with ozonesonde data in Figure 23. The model captures well the observed vertical gradients in the extratropics but not in the tropics. Ozonesonde data show a steep decrease of ozone concentrations in the tropical lower troposphere because of the semipermanent trade wind inversion [Heikes *et al.*, 1996; Logan, manuscript in preparation, 1998; Hastenrath, 1991]; this decrease is almost nonexistent in the model. The chemical lifetime of ozone in the tropical marine boundary layer is about 1 week in the model [Wang *et al.*, this issue(b)], consistent with inferences from observations [Johnson *et al.*, 1990; Heikes *et al.*, 1996]. We conclude that the model has excessive vertical mixing across the trade wind inversion. This excessive mixing leads in turn to an underestimate of ozone concentrations in the tropical free troposphere because of the shorter lifetime of ozone against chemical loss in the boundary layer than at higher altitudes.

Figure 23

9. Global Ozone Budget

The generally good simulations of ozone, NO , and H_2O_2 and the lifetime of tropospheric CH_3CCl_3 offer support for the representation of HO_x and NO_x chemistry in the model and lend confidence in applying the model to investigate tropospheric ozone budgets. The global budget in the model is shown in Table 1. The budget is given for the odd oxygen family ($\text{O}_x = \text{O}_3 + \text{O} + \text{NO}_2 + \text{HNO}_4 + 2 \times \text{NO}_3 + 3 \times \text{N}_2\text{O}_5 + \text{PANs} + \text{HNO}_3$), to account for the interconversion between ozone and other O_x species. Since ozone normally accounts for over 95% of O_x , we can view the budgets of ozone and O_x as effectively equivalent. The main source of O_x in the troposphere is the reaction of peroxy radicals with NO ; the main sinks are the reactions $\text{O}^1D + \text{H}_2\text{O}$, $\text{O}_3 + \text{HO}_2$, and $\text{O}_3 + \text{HO}_2$. We also calculated the ozone loss by applying the O_x loss frequencies in the model to a climatology of observed tropospheric ozone distributions (Logan, manuscript in preparation, 1998). The resulting global ozone loss was 6% lower than the estimate of Table 1.

Table 1

We see in Table 1 that sources and sinks of tropospheric ozone are dominated by photochemistry within the troposphere. Although transport from the stratosphere contributes less than 10% of the global source of ozone in the troposphere, its actual contribution to the tropospheric ozone inventory is somewhat larger because of the relatively long lifetime of ozone in the extratropical troposphere, where cross-tropopause

transport takes place. This issue and other features of the tropospheric ozone budget are discussed by Wang *et al.* [this issue(b)].

We find that the tropospheric ozone inventory is 40% larger in the northern hemisphere than in the southern hemisphere, although NO_x emissions are 3 times larger in the northern hemisphere. Liu *et al.* [1987] showed that the number of O_x molecules produced per NO_x molecule emitted (ozone production efficiency) decreases with increasing NO_x concentrations. Our model yields annual mean values for the ozone production efficiency of 28 mol/mol globally, 23 mol/mol in the northern hemisphere, and 46 mol/mol in the southern hemisphere. Thus NO_x emitted in the southern hemisphere is twice as efficient at producing ozone as NO_x emitted in the northern hemisphere.

Our global ozone budget can be compared with previous three-dimensional model results from Müller and Brasseur [1995] (MB95), Roelofs and Lelieveld [1995] (RL95), and Crutzen [1994] (C94). Our chemical production and loss rates averaged globally and annually are 10% lower than MB95, 5% (production) and 15% (loss) higher than C94, and 30% higher than RL95. The lower production rates of C94 and RL95 could be due in part to their omission of NMHCs; without NMHCs the production rate in our model would be 10% lower [Wang *et al.*, this issue(b)]. The budget domain used by MB95 extends up to 50 mbar, as compared with 150 mbar in our model, accounting for the significantly longer residence time in their model (120 days) than in our model (25 days). The ozone loss by dry deposition in our model is 10% higher than RL95 but 25% lower than MB95 and 40% lower than C94. Ozone deposition velocities in C94 are fixed at 0.4 cm s^{-1} over land and 0.1 cm s^{-1} over oceans [Crutzen and Zimmermann, 1991], which appear to be too high [Wang *et al.*, this issue(a)].

10. Conclusions

We have presented a detailed evaluation of a global three-dimensional model of tropospheric chemistry using surface, ozonesonde, and aircraft measurements of ozone, NO, PAN, HNO_3 , CO, ethane, acetone, and H_2O_2 . The model generally captures the observed seasonal variations and regional distributions of these species, although there are a number of discrepancies. The global mean OH concentration computed in the model compares well with the estimate using CH_3CCl_3 as a proxy [Prinn *et al.*, 1995]. We summarize here some particularly interesting results of the model evaluation.

The model reproduces observed NO and PAN concentrations to within a factor of 2 in most tropospheric regions but tends to overestimate HNO_3 concentrations in the remote troposphere, often several fold. Previous authors have hypothesized rapid conversion of HNO_3 to NO_x by an unknown mechanism in order to reconcile photochemical equilibrium model calculations with observed HNO_3/NO_x ratios in the remote troposphere [Chatfield, 1994; Fan *et al.*, 1994; Hauglustaine *et al.*, 1996; Jacob *et al.*, 1996]. We find, however, in our model that recycling of HNO_3 to NO_x at the rate needed to match HNO_3 concentrations would lead to large overestimates

of NO concentrations everywhere except in the upper troposphere over the tropical South Atlantic (an area influenced strongly by biomass burning). Aside from this exception, it appears necessary to invoke HNO₃ sinks that do not lead to rapid recycling of NO_x. There are also concerns regarding the quality of the HNO₃ measurements [Crosley, 1996].

Acetone appears to provide a major source of HO_x in the upper troposphere [Singh *et al.*, 1995; Jaegle *et al.*, 1997; McKeen *et al.*, 1997], but its sources are not understood. We can reproduce available observations for atmospheric acetone in our model by including a biogenic source of 15 Tg C yr⁻¹, which then accounts for 40% of our global acetone source of 37 Tg C yr⁻¹ [Wang *et al.*, this issue(a)]. This biogenic source can explain the relatively high acetone concentrations observed in tropical regions remote from biomass burning influence [Singh *et al.*, 1995]. The persistence of high acetone concentrations in the upper troposphere reflects the long lifetime of acetone against photolysis at low altitudes (1-2 months in surface air versus 2-3 weeks at 300 mbar in the tropics).

A prominent feature of ozone observations in the lower troposphere of northern midlatitudes is the summer maximum at polluted sites and the spring maximum at remote sites [Logan, 1985; Levy *et al.*, 1985]. The model reproduces this seasonality. The summer maximum at polluted sites reflects rapid photochemical production when UV radiation is strongest, while the spring maximum at remote sites reflects a combination of photochemical and stratospheric influence as discussed by Wang *et al.* [this issue(b)]. Seasonal variations of ozone in other regions of the troposphere are also well simulated by the model. An exception is the winter maximum in surface air at southern high latitudes, which is shifted to spring in the model as a result of excessive subsidence of biomass burning pollution transported from the tropics. The model tends to overestimate ozone concentrations in the tropical marine boundary layer; this problem appears to be caused by excessive vertical mixing across the trade wind inversion.

Overall, the ability of the model to reproduce observations for ozone, NO, and H₂O₂ (proxy for HO_x radicals) and the lifetime of CH₃CCl₃ (proxy for the global mean OH) lends confidence in using the model to understand the factors controlling tropospheric ozone. A global budget presented in this paper shows that the source of tropospheric ozone is dominated by chemical production within the troposphere (4100 Tg O₃ yr⁻¹, compared with 400 Tg yr⁻¹ for transport from the stratosphere) and the sink is dominated by chemical loss (3700 Tg yr⁻¹, compared with 800 Tg yr⁻¹ for deposition). The inter-hemispheric difference in the ozone inventory is much less than the disparity in NO_x emissions, reflecting a higher ozone production efficiency for NO_x emitted in the southern hemisphere than in the northern hemisphere (46 mol/mol versus 23 mol/mol). Further discussion of factors controlling tropospheric ozone concentrations is presented by Wang *et al.* [this issue(b)].

Acknowledgments. This work benefited greatly from many discussions we had with Clarissa Spivakovsky. We thank Scott Smyth at Georgia Institute of Technology and NASA Langley Center for pro-

viding the compilation of aircraft data used in our model evaluation. We also thank Amy Alberts and Dan Cohan for processing ozone-sonde data. We would like to acknowledge the helpful comments from two anonymous reviewers. This work was supported by the National Aeronautics and Space Administration (NASA-NAGI-1909, NASA-NAGS-2688, and NASA-NAG5-3553), the Environmental Protection Agency (EPA-R824096-01-0), and the National Science Foundation (ATM-9612282).

References

- Andreae, M. O., A. Chapuis, B. Cros, J. Fontan, G. Helas, C. Justice, Y. J. Kaufman, A. Minga, and D. Nganga, Ozone and Aitken nuclei over equatorial Africa: Airborne observations during DECAFE 88, *J. Geophys. Res.*, **97**, 6137-6148, 1992.
- Atkinson, R. A., D. L. Baulch, R. A. Cox, R. F. Hampson, Jr., J. A. Kerr, and J. Troe, Evaluated kinetic and photochemical data for atmospheric chemistry, supplement IV, IUPAC subcommittee on gas kinetic data evaluation for atmospheric chemistry, *J. Phys. Chem. Ref. Data*, **21**, 1125-1568, 1992.
- Bakwin, P. S., S. C. Wofsy, S.-M. Fan, M. Keller, S. Trumbore, and J. M. da Costa, Emission of nitric oxide (NO) from tropical forest soils and exchange of NO between the forest canopy and atmospheric boundary layers, *J. Geophys. Res.*, **95**, 16,755-16,764, 1990.
- Balkanski, Y. J., D. J. Jacob, G. M. Gardner, W. M. Graustein, and K. K. Turekian, Transport and residence times of continental aerosols inferred from a global three-dimensional simulation of ^{210}Pb , *J. Geophys. Res.*, **98**, 20,573-20,586, 1993.
- Barrie, L. A., J. W. Bottenheim, R. C. Schnell, P. J. Crutzen, and R. A. Rasmussen, Ozone destruction and photochemical reactions at polar sunrise in the lower Arctic atmosphere, *Nature*, **334**, 138-140, 1988.
- Blake, D. R., D. F. Hurst, T. W. Smith, Jr., W. J. Wipple, T.-Y. Chen, N. J. Blake, and F. S. Rowland, Summertime measurements of selected nonmethane hydrocarbons in the Arctic and subArctic during the 1988 Arctic Boundary Layer Expedition (ABLE 3A), *J. Geophys. Res.*, **97**, 16,559-16,588, 1992.
- Bottenheim, J. W., and M. F. Shepherd, $\text{C}_2\text{-C}_6$ hydrocarbon measurements at four rural locations across Canada, *Atmos. Environ.*, **29**, 647-664, 1995.
- Bradshaw, J., S. B. Smyth, S. C. Liu, R. Newell, D. D. Davis, and S. T. Sandholm, Observed distributions of nitrogen oxides in the remote free troposphere from NASA Global Tropospheric Experiments, in press, *Rev. Geophys.*, 1998.
- Browell, E. V., et al., Ozone and aerosol distributions and air mass characteristics over the South Atlantic Basin during the burning season, *J. Geophys. Res.*, **101**, 24,043-24,068, 1996.
- Chatfield, R. B., Anomalous HNO_3/NO_x ratio of remote tropospheric air: Conversion of nitric acid to formic acid and NO_x , *Geophys. Res. Lett.*, **21**, 2705-2708, 1994.
- Chin, M., D. J. Jacob, G. M. Gardner, M. S. Forman-Fowler, P. A. Spiro, and D. L. Savoie, A global three-dimensional model of tropospheric sulfate, *J. Geophys. Res.*, **101**, 18,667-18,690, 1996.
- Crawford, J., et al., Photostationary state analysis of the $\text{NO}_2\text{-NO}$ system based on airborne observations from the western and central North Pacific, *J. Geophys. Res.*, **101**, 2053-2072, 1996.
- Cros, B., R. Delmas, B. Clairac, J. Loemba-Ndembu, and J. Fontan, Survey of ozone concentrations in an equatorial region during the rainy season, *J. Geophys. Res.*, **92**, 9772-9778, 1987.
- Crosley, D. R., NO_y blue ribbon panel, *J. Geophys. Res.*, **101**, 2049-2052, 1996.
- Crutzen, P. J., Global tropospheric chemistry, in *Low-Temperature Chemistry of the Atmosphere*, NATO ASI Ser., vol. 121, edited by G. K. Moortgat et al., pp. 465-498, Springer-Verlag, New York, 1994.
- Crutzen, P. J., and P. H. Zimmermann, The changing photochemistry of the troposphere, *Tellus*, **43AB**, 136-151, 1991.
- Dentener, F. J., and P. J. Crutzen, Reaction of N_2O_5 on tropospheric aerosols: Impact on the global distributions of NO_x , O_3 , and OH, *J. Geophys. Res.*, **98**, 7149-7163, 1993.
- Drummond, J. W., D. H. Ehhalt, and A. Voltz, Measurement of nitric oxide between 0-12 km altitude and 67°N and 60°S latitude obtained during STRATOZ III, *J. Geophys. Res.*, **93**, 15,831-15,849, 1988.
- Emmons, L. K., et al., Climatologies of NO_x and NO_y : A comparison of data and models, *Atmos. Environ.*, **31**, 1851-1903, 1997.
- Fan, S.-M., D. J. Jacob, D. L. Mauzerall, J. D. Bradshaw, S. T. Sandholm, D. R. Blake, H. B. Singh, R. W. Talbot, G. L. Gregory, and

- G. W. Sachse, Photochemistry of reactive nitrogen in the subArctic troposphere in summer 1990: Observation and modeling, *J. Geophys. Res.*, **99**, 16,867-16,878, 1994.
- Fishman, J., F. Fakhruzzaman, B. Cros, and D. Nganga, Identification of widespread pollution in the southern hemisphere from satellite analysis, *Science*, **252**, 1693-1696, 1991.
- Fishman, J., J. M. Hoell, Jr., R. D. Bendura, V. W. J. H. Kirchhoff, and R. J. McNeal, Jr., The NASA GTE TRACE-A Experiment (September-October 1992): Overview, *J. Geophys. Res.*, **101**, 23,865-23,879, 1996.
- Goldstein, A. H., S. C. Wofsy, and C. M. Spivakovsky, Seasonal variations of nonmethane hydrocarbons in rural New England: Constraints on OH concentrations in northern midlatitudes, *J. Geophys. Res.*, **100**, 21,023-21,033, 1995.
- Hansen, J., G. Russel, D. Rind, P. Stone, A. Lacis, S. Lebedeff, R. Ruedy, and L. Travis, Efficient three-dimensional global models for climate studies: Models I and II, *Mon. Weather Rev.*, **111**, 609-662, 1983.
- Hastenrath, S., *Climate Dynamics of the Tropics*, chap. 6, pp. 114-218, Kluwer Acad., Norwell, Mass., 1991.
- Hauglustaine, D. A., B. A. Ridley, S. Solomon, P. G. Hess, and S. Madronich, HNO_3/NO_x ratio in the remote troposphere during MLOPEX 2: Evidence for nitric acid reduction on carbonaceous aerosols?, *Geophys. Res. Lett.*, **23**, 2609-2612, 1996.
- Heikes, B., M. Lee, D. J. Jacob, R. Talbot, J. Bradshaw, H. Singh, D. Blake, B. Anderson, H. Fuelberg, and A. M. Thompson, Ozone, hydroperoxides, oxides of nitrogen, and hydrocarbon budgets in the marine boundary layer over the South Atlantic, *J. Geophys. Res.*, **101**, 24,221-24,234, 1996.
- Helas, G., et al., Airborne measurements of savanna fire emissions and the regional distribution of pyrogenic pollutants over western Africa, *J. Atmos. Chem.*, **22**, 217-239, 1995.
- Holton, J. R., P. H. Haynes, M. E. McIntyre, A. R. Douglass, R. B. Rood, and L. Pfister, Stratosphere-troposphere exchange, *Rev. Geophys.*, **33**, 403-439, 1995.
- Horowitz, L. W., J. Liang, G. M. Gardner, and D. J. Jacob, Export of reactive nitrogen from North America during summertime, *J. Geophys. Res.*, in press, 1998.
- Jacob, D. J., and S. C. Wofsy, Photochemistry of biogenic emissions over the Amazon forest, *J. Geophys. Res.*, **93**, 1477-1486, 1988.
- Jacob, D. J., and S. C. Wofsy, Budgets of reactive nitrogen, hydrocarbons, and ozone over the Amazon forest during the wet season, *J. Geophys. Res.*, **95**, 16,737-16,754, 1990.
- Jacob, D. J., et al., Summertime photochemistry of the troposphere at high northern latitudes, *J. Geophys. Res.*, **97**, 16,421-16,431, 1992.
- Jacob, D. J., et al., Simulation of summertime ozone over North America, *J. Geophys. Res.*, **98**, 14,797-14,816, 1993.
- Jacob, D. J., et al., The origin of ozone and NO_x in the tropical troposphere: A photochemical analysis of aircraft observations over the South Atlantic Basin, *J. Geophys. Res.*, **101**, 24,235-24,250, 1996.
- Jaegle, L., et al., Observed OH and HO_2 in the upper troposphere suggest a major source from convective injection of peroxides, *Geophys. Res. Lett.*, **24**, 3181-3184, 1997.
- Johnson, J. E., R. H. Gammon, J. Larsen, T. S. Bates, S. J. Oltmans, and J. C. Farmer, Ozone in the marine boundary layer over the Pacific and Indian Oceans: Latitudinal gradient and diurnal cycles, *J. Geophys. Res.*, **95**, 11,847-11,856, 1990.
- Kanakidou, M., and P. J. Crutzen, Scale problems in global tropospheric chemistry modeling: Comparison of results obtained with a three dimensional model, adopting longitudinally uniform and varying emissions of NO_x and NMHC, *Chemosphere*, **26**, 787-801, 1993.
- Koch, D. M., D. J. Jacob, and W. G. Graustein, Vertical transport of tropospheric aerosols as indicated by ^7Be and ^{210}Pb in a chemical tracer model, *J. Geophys. Res.*, **101**, 18,651-18,666, 1996.
- Lee, M., B. G. Heikes, D. J. Jacob, G. Satche, and B. Anderson, Hydrogen peroxide, organic hydroperoxide, and formaldehyde as primary pollutants from biomass burning, *J. Geophys. Res.*, **102**, 1301-1309, 1997.
- Levy, H., II, Normal atmosphere: Large radical and formaldehyde concentrations predicted, *Science*, **173**, 141-143, 1971.

- Levy, H., II, J. D. Mahlman, W. J. Moxim, and S. C. Liu, Tropospheric ozone: The role of transport, *J. Geophys. Res.*, **90**, 3753-3772, 1985.
- Liang, J., L. W. Horowitz, D. J. Jacob, Y. Wang, A. M. Fiore, J. A. Logan, G. M. Gardner, and J. W. Munger, Seasonal variation of photochemistry over North America and its implications for the export of ozone and reactive nitrogen to the global atmosphere, *J. Geophys. Res.*, in press, 1998.
- Lindskog, A., and J. Moldanova, The influence of the origin, season, and time of the day on the distribution of individual NMHC measured at Rorvik, Sweden, *Atmos. Environ.*, **28**, 2383-2398, 1994.
- Liu, S. C., M. Trainer, F. C. Fehsenfeld, D. D. Parrish, E. J. Williams, D. W. Fahey, G. Hubler, and P. C. Murphy, Ozone production in the rural troposphere and the implications for regional and global ozone distributions, *J. Geophys. Res.*, **92**, 10,463-10,471, 1987.
- Lobert, J. M., D. H. Scharffe, W.-M. Hao, T. A. Kuhlbusch, R. Seuwen, P. Warneck, and P. J. Crutzen, Experimental evaluation of biomass burning emissions: Nitrogen and carbon compounds, in *Global Biomass Burning: Atmospheric, Climatic and Biospheric Implications*, edited by J. S. Levine, MIT Press, Cambridge, Mass., 1991.
- Logan, J. A., Tropospheric ozone: Seasonal behavior, trends, and anthropogenic influence, *J. Geophys. Res.*, **90**, 10,463-10,482, 1985.
- McKeen, S. A., T. Gierczak, J. B. Burkholder, P. O. Wennberg, T. F. Hanisco, E. R. Keim, A. R.-S. Gao, S. C. Liu, A. R. Ravishankara, and D. W. Fahey, The photochemistry of acetone in the upper troposphere: A source of odd-hydrogen radicals, *Geophys. Res. Lett.*, **24**, 3177-3180, 1997.
- Moxim, W. J., H. Levy II, and P. S. Kashibhatla, Simulated global tropospheric PAN: Its transport and impact on NO_x , *J. Geophys. Res.*, **101**, 12,621-12,638, 1996.
- Müller, J.-F., and G. Brasseur, IMAGES: A three-dimensional chemical transport model of the global troposphere, *J. Geophys. Res.*, **100**, 16,445-16,490, 1995.
- Munger, J. W., S. M. Fan, P. S. Bakwin, M. L. Goulden, A. H. Goldstein, A. S. Colman, and S. C. Wofsy, Regional budgets for nitrogen oxides from continental sources: Variations of rates for oxidation and deposition with season and distance from source regions, in press, *J. Geophys. Res.*, 1998.
- Novelli, P. C., L. P. Steele, and P. P. Tans, Mixing ratios of carbon monoxide in the troposphere, *J. Geophys. Res.*, **97**, 20,731-20,750, 1992.
- Novelli, P. C., J. E. Collins, Jr., R. C. Myers, G. W. Sachse, and H. E. Scheel, Reevaluation of the NOAA/CMDL carbon monoxide reference scale and comparisons to CO reference gases at NASA Langley and the Fraunhofer Institute, *J. Geophys. Res.*, **99**, 12,833-12,839, 1994.
- Oltmans, S. J., and H. Levy II, Surface ozone measurements from a global network, *Atmos. Environ.*, **28**, 9-24, 1994.
- Parrish, D. D., et al., The total reactive oxidized nitrogen levels and the partitioning between the individual species at six rural sites in eastern North America, *J. Geophys. Res.*, **98**, 2927-2939, 1993.
- Prather, M., and C. M. Spivakovsky, Tropospheric OH and the lifetime of hydrochlorofluorocarbons, *J. Geophys. Res.*, **95**, 18,723-18,729, 1990.
- Prinn, R. G., D. Cunnold, R. Rasmussen, P. Simmonds, F. Alyea, A. Crawford, P. Fraser, and R. Rosen, Atmospheric trends in methylchloroform and the global average for the hydroxyl radical, *Science*, **238**, 945-950, 1987.
- Prinn, R. G., R. F. Weiss, B. R. Miller, J. Huang, F. N. Alyea, D. M. Cunnold, P. J. Fraser, D. E. Hartley, and P. G. Simmonds, Atmospheric trends and lifetime of CH_3CCl_3 and global OH concentrations, *Science*, **269**, 187-192, 1995.
- Rinsland, C. P., N. B. Jones, and W. A. Matthews, Infrared spectroscopic measurements of the total column abundance of ethane (C_2H_6) above Lauder, New Zealand, *J. Geophys. Res.*, **99**, 25,941-25,945, 1994.
- Roelofs, G.-J., and J. Lelieveld, Distribution and budget of O_3 in the troposphere calculated with a chemistry general circulation model, *J. Geophys. Res.*, **100**, 20,983-20,998, 1995.

- Rudolph, J., The tropospheric distribution and budget of ethane, *J. Geophys. Res.*, *100*, 11,369-11,381, 1995.
- Rudolph, J., A. Khedim, and D. Wagenbach, The seasonal variation of light nonmethane hydrocarbons in the Antarctic troposphere, *J. Geophys. Res.*, *94*, 13,039-13,044, 1989.
- Singh H. B., D. O'Hara, D. Herlth, W. Sachse, D. R. Blake, J. D. Bradshaw, M. Kanakidou, and P. J. Crutzen, Acetone in the atmosphere: Distribution, sources, and sinks, *J. Geophys. Res.*, *99*, 1805-1819, 1994.
- Singh H. B., M. Kanakidou, P. J. Crutzen, and D. J. Jacob, High concentrations and photochemical fate of oxygenated hydrocarbons in the global troposphere, *Nature*, *378*, 50-54, 1995.
- Singh H. B., et al., Reactive nitrogen and ozone over the western Pacific: Distribution, partitioning, and sources, *J. Geophys. Res.*, *101*, 1793-1808, 1996.
- Smyth, S.B., et al., Factors influencing the upper free tropospheric distribution of reactive nitrogen over the South Atlantic during the TRACE-A Experiment, *J. Geophys. Res.*, *101*, 24,165-24,186, 1996.
- Talukdar, R. K., J. B. Burkholder, A. M. Schmoltner, J. M. Roberts, R. R. Wilson, and A. R. Ravishankara, Investigation of the loss processes for peroxyacetyl nitrate in the atmosphere: UV photolysis and reaction with OH, *J. Geophys. Res.*, *100*, 14,163-14,173, 1995.
- Thompson, A. M., The oxidizing capacity of the Earth's atmosphere: Probable past and future changes, *Science*, *256*, 1157-1165, 1992.
- Wang, Y., D. J. Jacob, and J. A. Logan, Global simulation of tropospheric O_3 - NO_x -hydrocarbon chemistry, 1, Model formulation, this issue(a).
- Wang, Y., D. J. Jacob, and J. A. Logan, Global simulation of tropospheric O_3 - NO_x -hydrocarbon chemistry, 3, Origin of tropospheric ozone and effects of nonmethane hydrocarbons, this issue(b).
- Wofsy, S. C., S.-M. Fan, D. R. Blake, J. D. Bradshaw, S. T. Sandholm, H. B. Singh, G. W. Sachse, and R. C. Harriss, Factors influencing atmospheric composition over subarctic North America during summer, *J. Geophys. Res.*, *99*, 1887-1897, 1994.

D. J. Jacob and J. A. Logan, Department of Earth and Planetary Sciences and Division of Engineering and Applied Sciences, Harvard University, Cambridge, MA 02138. (e-mail: djj@io.harvard.edu; jal@io.harvard.edu)

Y. Wang, School of Earth and Atmospheric Sciences, Georgia Institute of Technology, Atlanta, GA 30332-0340. (e-mail: yhw@eas.gatech.edu)

(Received June 2, 1997; revised January 5, 1998;
accepted January 9, 1998.)

¹Now at School of Earth and Atmospheric Sciences, Georgia Institute of Technology, Atlanta, Georgia.

Copyright 1998 by the American Geophysical Union.

Paper number 98JD00157.
0148-0227/98/98JD-00157\$09.00

Table 1. Global Budget for Tropospheric Ozone

	Global	Northern Hemisphere	Southern Hemisphere
<hr/>			
Sources, Tg O ₃ yr ⁻¹			
In situ chemical production ^a	4100	2620	1480
Transport from stratosphere	400	240	160
Total	4500	2860	1640
Sinks, Tg O ₃ yr ⁻¹			
In situ chemical loss ^b	3680	2290	1390
Dry deposition	820	530	290
Total	4500	2820	1680
Interhemispheric transport, Tg O ₃ yr ⁻¹	0	-40	40
Burden, Tg O ₃	310	180	130
Residence time, days	25	23	28
<hr/>			

The budget is for the air column extending up to 150 mbar. Annual mean budget terms are given for the odd oxygen family ($O_x = O_3 + O + NO_2 + HNO_4 + 2 \times NO_3 + 3 \times N_2O_5 + PANs + HNO_3$) to account for chemical interconversion between ozone and other components of O_x . Since ozone accounts for over 95% of O_x , the budgets of ozone and O_x can be regarded as equivalent.

^aMainly from the reactions of peroxy radicals with NO.

^bMainly from the reactions $O(^1D) + H_2O$, $O_3 + HO_2$, and $O_3 + OH$.

Figure Captions (Single Column)

Figure 1. Surface ozone and ozonesonde measurements used for model evaluation [Oltmans and Levy, 1994; J. A. Logan, An analysis of ozonesonde data, 1, Its application in testing models of tropospheric chemistry, manuscript in preparation, 1998; Liang *et al.*, 1998].

Figure 2. Regional aggregation of aircraft observations used for model evaluation: 1, Alaska in July; 2, central Canada in July; 3, eastern Canada in July; 4, U.S. west coast in August; 5, western U.S. in August; 6, eastern U.S. in August; 7, Amazonia in August; 8, Amazonia in May; 9, eastern Brazil in September; 10, Brazil south coast in September; 11, tropical South Atlantic in September; 12, African west coast in September; 13, southern Africa in September; 14, Japan coast in October; 15, East China Sea in October; 16, tropical western Pacific in October; 17, Hawaii in October; 18, Norway in February; 19, northeastern Pacific in February; 20, Japan coast in February; 21, East China Sea in February; 22, western Pacific in February; 23, western equatorial Pacific in February; 24, New Guinea in February. The compiled observations were obtained with a resolution of 1° latitude \times 1° longitude \times 1-km altitude from Scott Smyth at Georgia Institute of Technology [Bradshaw *et al.*, 1998, and references therein].

Figure 3. Simulated zonal mean OH concentrations (10^5 molecules cm^{-3}) in January and July.

Figure 4. Simulated monthly mean NO_x concentrations (pptv) near the surface and at 500 mbar for January and July.

Figure 5. Comparison of observed and simulated vertical profiles of NO concentrations in daytime (solar elevation above 5°) for the regions shown in Figure 2. The region numbers as defined in Figure 2 are shown in parentheses. The observations are binned vertically in 1-km intervals. Open squares and solid lines are median observations, with standard deviations represented by solid horizontal bars. Open circles are means of observations. Open triangles and dashed lines are the medians of monthly mean concentrations in the model for the ensemble of grid boxes composing the regions. Pluses and dashed horizontal bars are the means and standard deviations for the model, respectively.

Figure 5. (continued)

Figure 6. Simulated monthly mean HNO_3 concentrations (pptv) near the surface and at 500 mbar for January and July.

Figure 7. Same as Figure 5 but for HNO_3 regional profiles.

Figure 7. (continued)

Figure 8. Sensitivity of NO and HNO_3 concentrations to rapid recycling of HNO_3 to NO_x in the upper troposphere. The left panels show the longitudinal distributions of observed and

simulated NO and HNO₃ concentrations at 8- to 12-km altitude and 0°-20°S latitude over the tropical South Atlantic in September (TRACE-A expedition). The right panels show the latitudinal distributions of the same quantities at 8-10 km and 140°-165°E longitude over the western Pacific in October (PEM West-A Expedition). Solid lines are medians of observations, and solid vertical bars are standard deviations. Short-dashed lines are medians of monthly means in the standard model simulation. Long-dashed lines are for the simulation including rapid recycling from HNO₃ to NO_x ($k = 0.3 \text{ day}^{-1}$).

Figure 9. Simulated monthly mean PAN concentrations (pptv) near the surface and at 500 mbar for January and July.

Figure 10. Same as Figure 5 but for PAN regional profiles.

Figure 10. (continued)

Figure 11. Simulated monthly mean CO concentrations (ppbv) near the surface and at 500 mbar for January and July.

Figure 12. Comparison of observed and simulated monthly mean CO concentrations at surface sites. Solid lines and open circles are observed values [Novelli *et al.*, 1992, 1994], and vertical bars are standard deviations. Dashed lines and open triangles are model values.

Figure 13. Same as Figure 5 but for ethane regional profiles.

Figure 13. (continued)

Figure 14. Simulated and observed seasonal variations of monthly mean ethane concentrations at four surface sites: Egbert, Canada, for 1991 [Bottenheim and Shepherd, 1995]; Harvard Forest, Massachusetts, for 1992-1994 [Goldstein *et al.*, 1995]; Rorvik, Sweden, for 1989-1990 [Lindskog and Moldanova, 1994]; and "Georg von Neumayer," Antarctica, for 1982-1985 [Rudolph *et al.*, 1989]. Symbols are the same as in Figure 12. Vertical bars are standard deviations in the measurements; crosses and long-dashed lines are results from a sensitivity simulation with 6 Tg C yr⁻¹ ethane emitted by biomass burning, as compared with 2.5 Tg C yr⁻¹ in the standard simulation (open triangles and short-dashed lines).

Figure 15. Observed total ethane column over Lauder, New Zealand, for 1993-1994 [Rinsland *et al.*, 1994] and simulated columns up to 150 mbar from the standard simulation and the simulation with 6 Tg C yr⁻¹ ethane emitted from biomass burning. Symbols are the same as in Figure 14.

Figure 16. Simulated monthly mean concentrations of acetone (pptv) near the surface and at 500 mbar for January and July.

Figure 17. Same as Figure 5 but for acetone regional profiles.

Figure 18. Simulated zonal mean concentrations of acetone (pptv) as a function of latitude and pressure. Values are aver-

ages for different seasons.

Figure 19. Simulated monthly mean H_2O_2 concentrations (pptv) near the surface and at 500 mbar for January and July.

Figure 20. Same as Figure 5 but for H_2O_2 regional profiles.

Figure 21. Simulated monthly mean ozone concentrations (ppbv) near the surface and at 500 mbar for January and July.

Figure 22a. Comparison of observed and simulated monthly mean ozone concentrations for the surface sites in Figure 1. Solid lines and open circles are observations; dashed lines and open triangles are model results. Observations are from *Oltmans and Levy* [1994], Logan (manuscript in preparation, 1998), and *Munger et al.* [1998]. The observations identified as Oregon, Indiana, Virginia, and Arizona are 1980-1994 averages over a $4^\circ \times 5^\circ$ model grid square of data from a number of sites reported by the Aeronomic Information Retrieval Service of the U.S. Environmental Protection Agency [*Liang et al.*, 1998]. Observations at these U.S. sites and at Harvard Forest are for 1300-1600 local time; observations at other sites are 24-hour averages.

Figure 22a. (continued)

Figure 22b. Comparison of observed and simulated ozone concentrations at 800 mbar for the ozonesonde sites in Figure 1. Symbols are the same as Figure 22a. Vertical bars are standard deviations in the observations. Data are from Logan (manuscript in preparation, 1998).

Figure 22b. (continued)

Figure 22c. Same as Figure 22b but at 500 mbar.

Figure 22c. (continued)

Figure 22d. Same as Figure 22b but at 300 mbar. For stations north of 35°N , stratospheric data were filtered out from each individual sonde profile using concurrent measurements of temperature (Logan, manuscript in preparation, 1998). For these sites the filtered tropospheric data are shown as solid circles and solid lines, and the unfiltered data are shown as long-dashed lines.

Figure 22d. (continued)

Figure 23. Comparison of observed and simulated seasonal mean vertical profiles of ozone concentrations for six representative ozonesonde sites (Figure 1). Solid lines are observations, filtered to remove stratospheric data at sites north of 35°N (long-dashed lines show the unfiltered data). Short-dashed lines are model results.

Figure 23. (continued)

Figure Captions (Double Column)

Figure 1. Surface ozone and ozonesonde measurements used for model evaluation [Oltmans and Levy, 1994; J. A. Logan, An analysis of ozonesonde data, 1, Its application in testing models of tropospheric chemistry, manuscript in preparation, 1998; Liang *et al.*, 1998].

Figure 2. Regional aggregation of aircraft observations used for model evaluation: 1, Alaska in July; 2, central Canada in July; 3, eastern Canada in July; 4, U.S. west coast in August; 5, western U.S. in August; 6, eastern U.S. in August; 7, Amazonia in August; 8, Amazonia in May; 9, eastern Brazil in September; 10, Brazil south coast in September; 11, tropical South Atlantic in September; 12, African west coast in September; 13, southern Africa in September; 14, Japan coast in October; 15, East China Sea in October; 16, tropical western Pacific in October; 17, Hawaii in October; 18, Norway in February; 19, northeastern Pacific in February; 20, Japan coast in February; 21, East China Sea in February; 22, western Pacific in February; 23, western equatorial Pacific in February; 24, New Guinea in February. The compiled observations were obtained with a resolution of 1° latitude \times 1° longitude \times 1-km altitude from Scott Smyth at Georgia Institute of Technology [Bradshaw *et al.*, 1998, and references therein].

Figure 3. Simulated zonal mean OH concentrations (10^5 molecules cm^{-3}) in January and July.

Figure 4. Simulated monthly mean NO_x concentrations (pptv) near the surface and at 500 mbar for January and July.

Figure 5. Comparison of observed and simulated vertical profiles of NO concentrations in daytime (solar elevation above 5°) for the regions shown in Figure 2. The region numbers as defined in Figure 2 are shown in parentheses. The observations are binned vertically in 1-km intervals. Open squares and solid lines are median observations, with standard deviations represented by solid horizontal bars. Open circles are means of observations. Open triangles and dashed lines are the medians of monthly mean concentrations in the model for the ensemble of grid boxes composing the regions. Pluses and dashed horizontal bars are the means and standard deviations for the model, respectively.

Figure 5. (continued)

Figure 6. Simulated monthly mean HNO_3 concentrations (pptv) near the surface and at 500 mbar for January and July.

Figure 7. Same as Figure 5 but for HNO_3 regional profiles.

Figure 7. (continued)

Figure 8. Sensitivity of NO and HNO_3 concentrations to rapid recycling of HNO_3 to NO_x in the upper troposphere. The left panels show the longitudinal distributions of observed and simulated NO and HNO_3 concentrations at 8- to 12-km altitude and 0° - 20°S latitude over the tropical South Atlantic in September (TRACE-A expedition). The right panels show the latitudinal distributions of the same quantities at 8-10 km and 140° - 165°E longitude over the western Pacific in October (PEM West-A Expedition). Solid lines are medians of observations, and solid vertical bars are standard deviations. Short-dashed lines are medians of monthly means in the standard model simulation. Long-dashed lines are for the simulation including rapid recycling from HNO_3 to NO_x ($k = 0.3 \text{ day}^{-1}$).

Figure 9. Simulated monthly mean PAN concentrations (pptv) near the surface and at 500 mbar for January and July.

Figure 10. Same as Figure 5 but for PAN regional profiles.

Figure 10. (continued)

Figure 11. Simulated monthly mean CO concentrations (ppbv) near the surface and at 500 mbar for January and July.

Figure 12. Comparison of observed and simulated monthly mean CO concentrations at surface sites. Solid lines and open circles are observed values [Novelli *et al.*, 1992, 1994], and vertical bars are standard deviations. Dashed lines and open triangles are model values.

Figure 13. Same as Figure 5 but for ethane regional profiles.

Figure 13. (continued)

Figure 14. Simulated and observed seasonal variations of monthly mean ethane concentrations at four surface sites: Egbert, Canada, for 1991 [Bottenheim and Shepherd, 1995]; Harvard Forest, Massachusetts, for 1992-1994 [Goldstein *et al.*, 1995]; Rorvik, Sweden, for 1989-1990 [Lindsog and Moldanova, 1994]; and “Georg von Neumayer,” Antarctica, for 1982-1985 [Rudolph *et al.*, 1989]. Symbols are the same as in Figure 12. Vertical bars are standard deviations in the measurements; crosses and long-dashed lines are results from a sensitivity simulation with 6 Tg C yr⁻¹ ethane emitted by biomass burning, as compared with 2.5 Tg C yr⁻¹ in the standard simulation (open triangles and short-dashed lines).

Figure 15. Observed total ethane column over Lauder, New Zealand, for 1993-1994 [Rinsland *et al.*, 1994] and simulated columns up to 150 mbar from the standard simulation and the simulation with 6 Tg C yr⁻¹ ethane emitted from biomass burning. Symbols are the same as in Figure 14.

Figure 16. Simulated monthly mean concentrations of acetone (pptv) near the surface and at 500 mbar for January and July.

Figure 17. Same as Figure 5 but for acetone regional profiles.

Figure 18. Simulated zonal mean concentrations of acetone (pptv) as a function of latitude and pressure. Values are averages for different seasons.

Figure 19. Simulated monthly mean H₂O₂ concentrations (pptv) near the surface and at 500 mbar for January and July.

Figure 20. Same as Figure 5 but for H₂O₂ regional profiles.

Figure 21. Simulated monthly mean ozone concentrations (ppbv) near the surface and at 500 mbar for January and July.

Figure 22a. Comparison of observed and simulated monthly mean ozone concentrations for the surface sites in Figure 1. Solid lines and open circles are observations; dashed lines and open triangles are model results. Observations are from Oltmans and Levy [1994], Logan (manuscript in preparation, 1998), and Munger *et al.* [1998]. The observations identified as Oregon, Indiana, Virginia, and Arizona are 1980-1994 averages over a 4°x5° model grid square of data from a number of sites reported by the Aeronomic Information Retrieval Service of the U.S. Environmental Protection Agency [Liang *et al.*, 1998]. Observations at these U.S. sites and at Harvard Forest are for 1300-1600 local time; observations at other sites are 24-hour averages.

Figure 22a. (continued)

Figure 22b. Comparison of observed and simulated ozone concentrations at 800 mbar for the ozonesonde sites in Figure 1. Symbols are the same as Figure 22a. Vertical bars are standard deviations in the observations. Data are from Logan (manuscript in preparation, 1998).

Figure 22b. (continued)

Figure 22c. Same as Figure 22b but at 500 mbar.

Figure 22c. (continued)

Figure 22d. Same as Figure 22b but at 300 mbar. For stations north of 35°N, stratospheric data were filtered out from each individual sonde profile using concurrent measurements of temperature (Logan, manuscript in preparation, 1998). For these sites the filtered tropospheric data are shown as solid circles and solid lines, and the unfiltered data are shown as long-dashed lines.

Figure 22d. (continued)

Figure 23. Comparison of observed and simulated seasonal mean vertical profiles of ozone concentrations for six representative ozonesonde sites (Figure 1). Solid lines are observations, filtered to remove stratospheric data at sites north of 35°N (long-dashed lines show the unfiltered data). Short-dashed lines are model results.

Figure 23. (continued)

Ozone Observation Sites

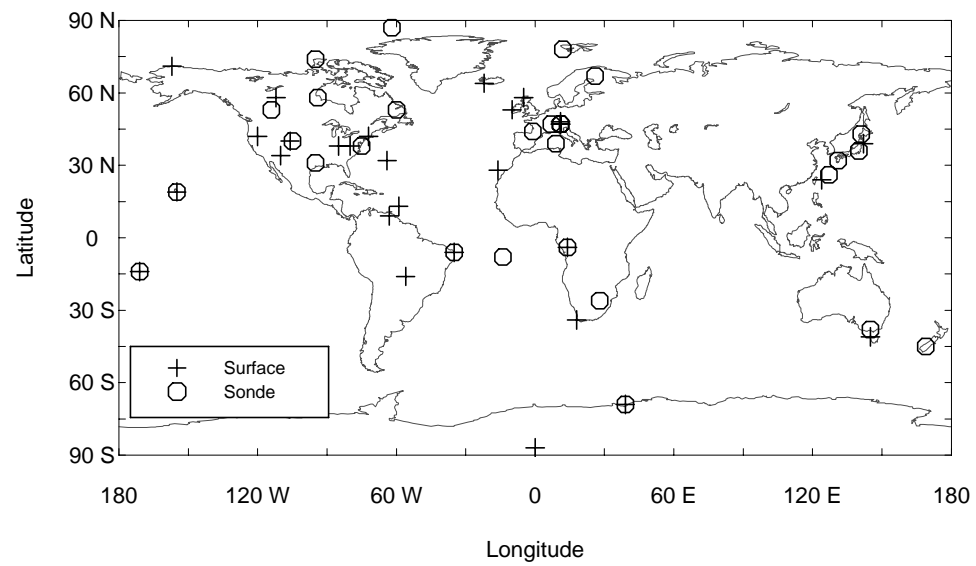


Fig. 1 (Bottom)

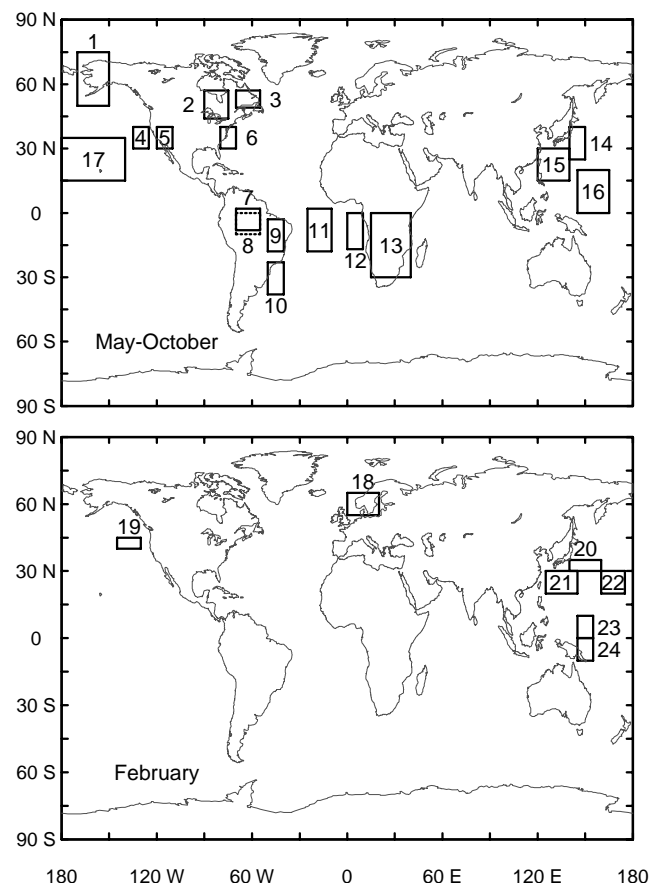


Fig. 2 (Bottom)

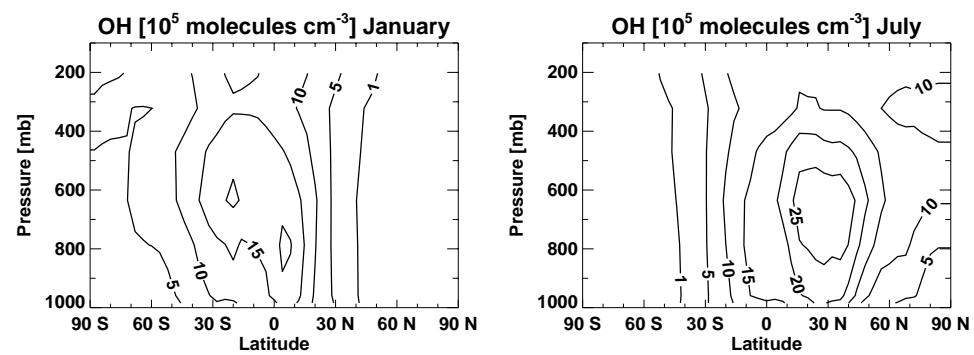
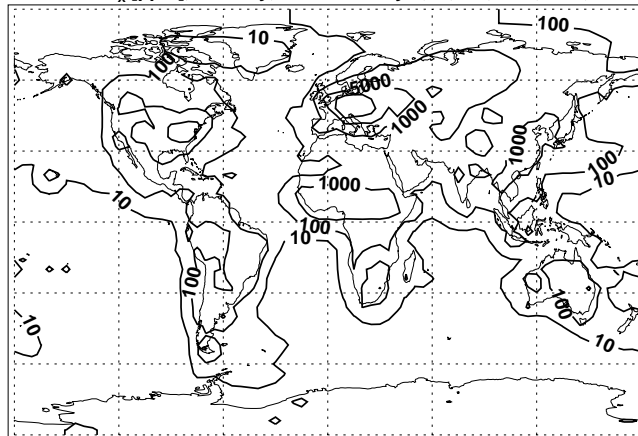
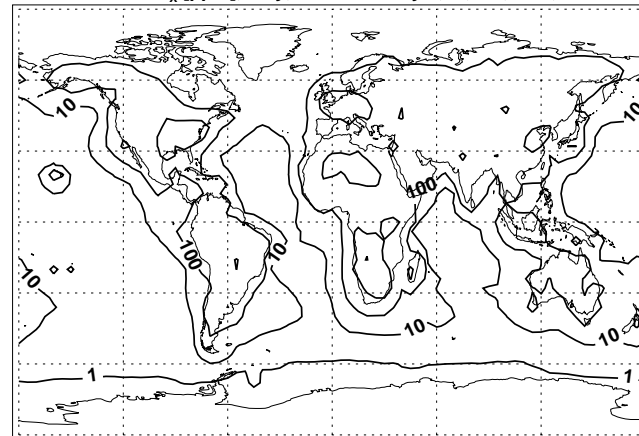


Fig. 3 (Bottom)

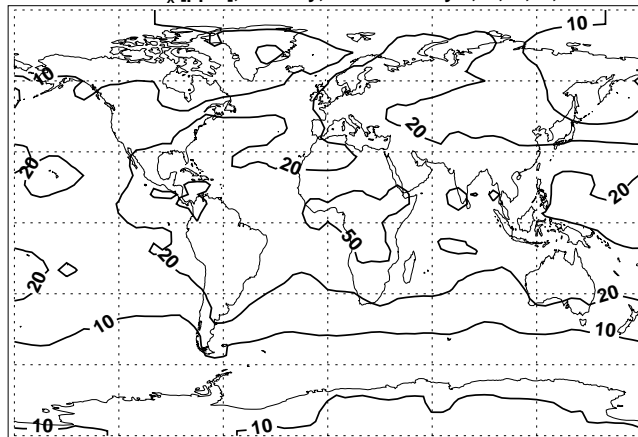
Surface NO_x [pptv], January, Contoured by 1,10,100,1000,5000,10000



Surface NO_x [pptv], July, Contoured by 1,10,100,1000,5000



500 mb NO_x [pptv], January, Contoured by 1,10,20,50,100



500 mb NO_x [pptv], July, Contoured by 1,10,20,50,100

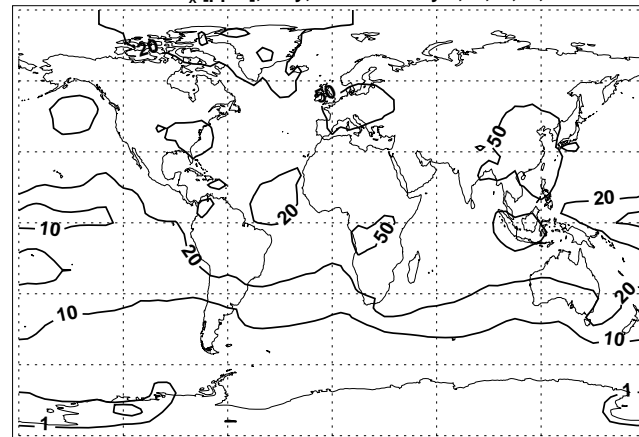


Fig. 4 (Bottom)

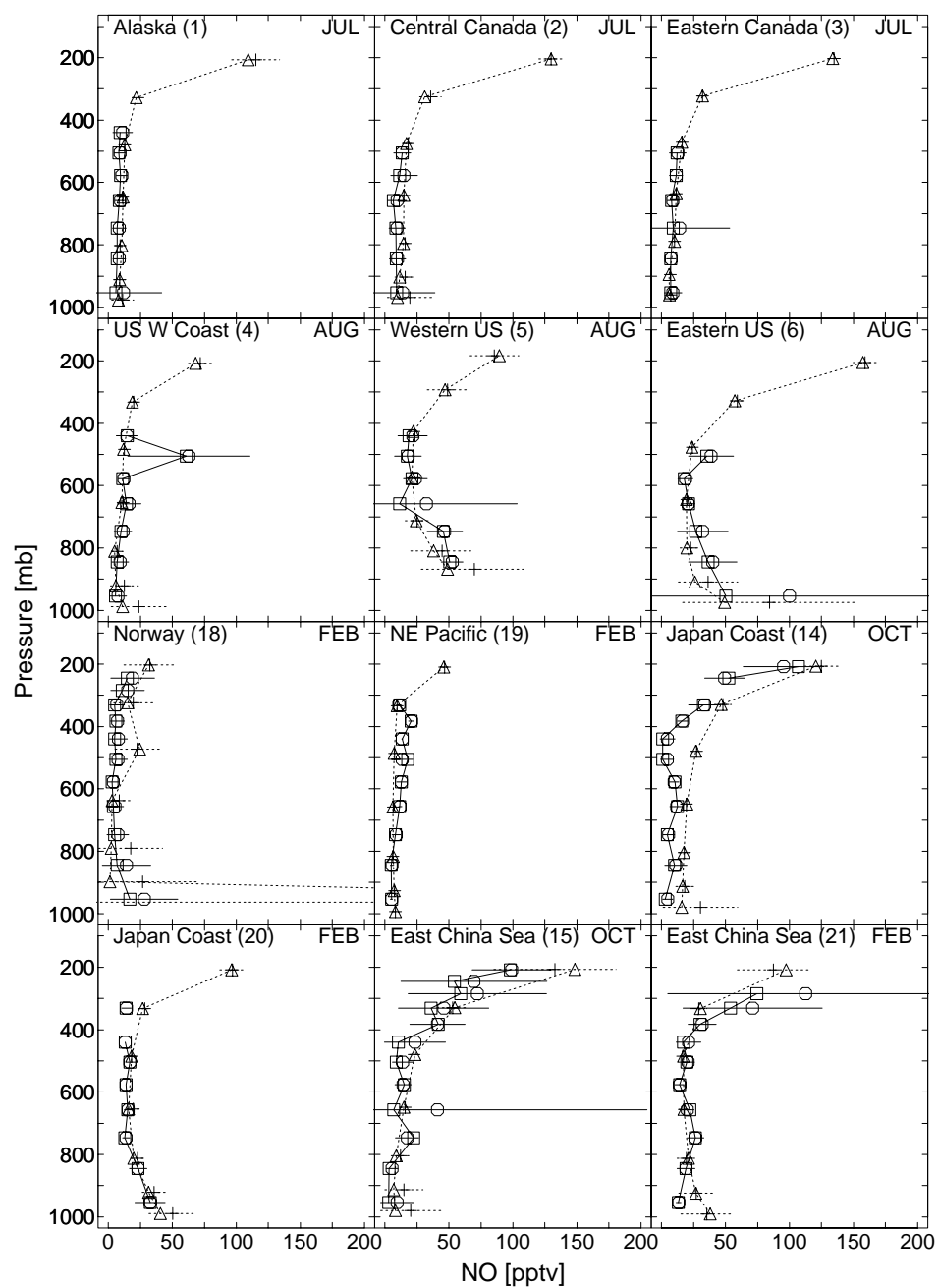


Fig. 5 (Bottom)

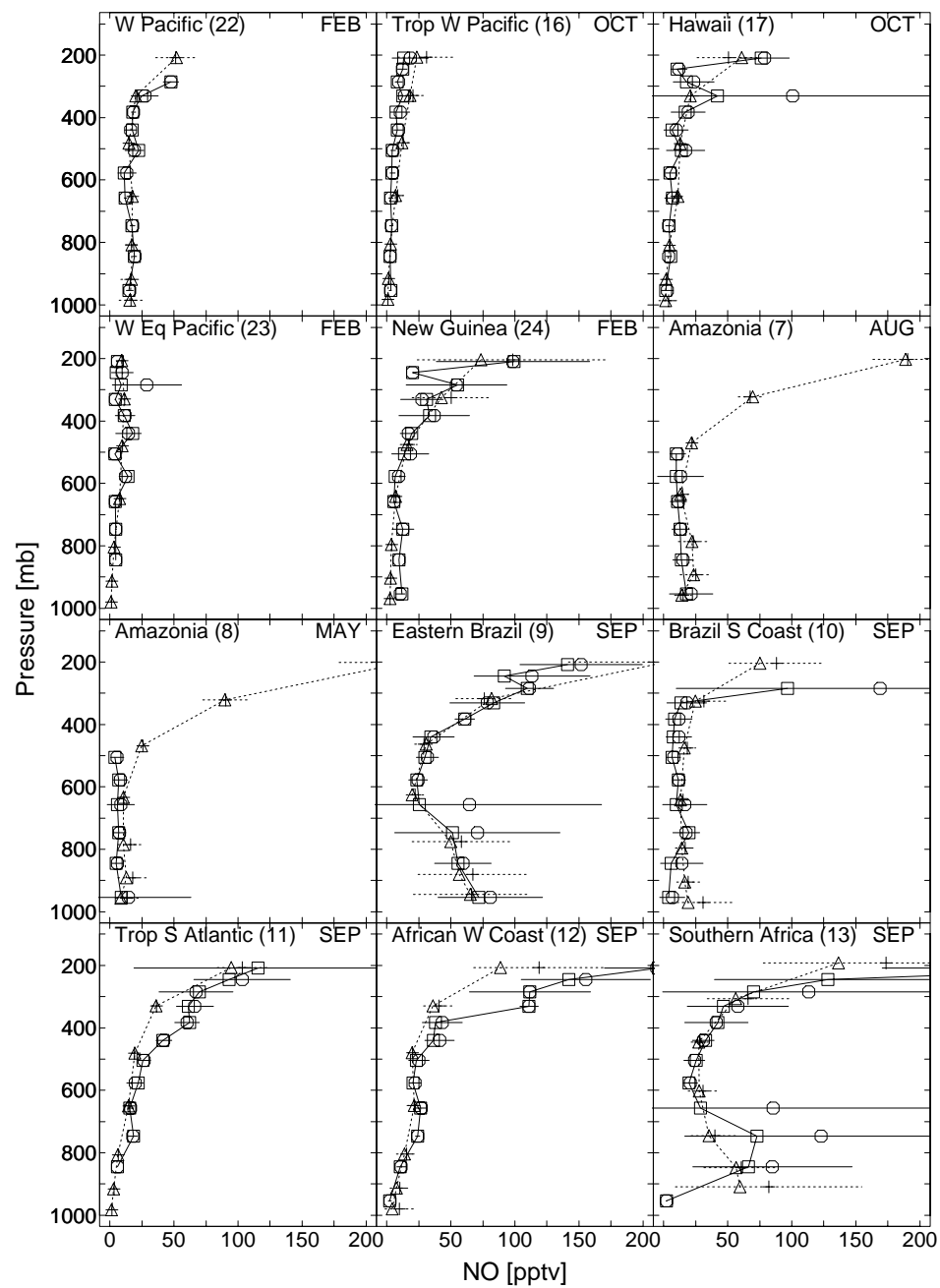


Fig. 5 (cont.) (Bottom)

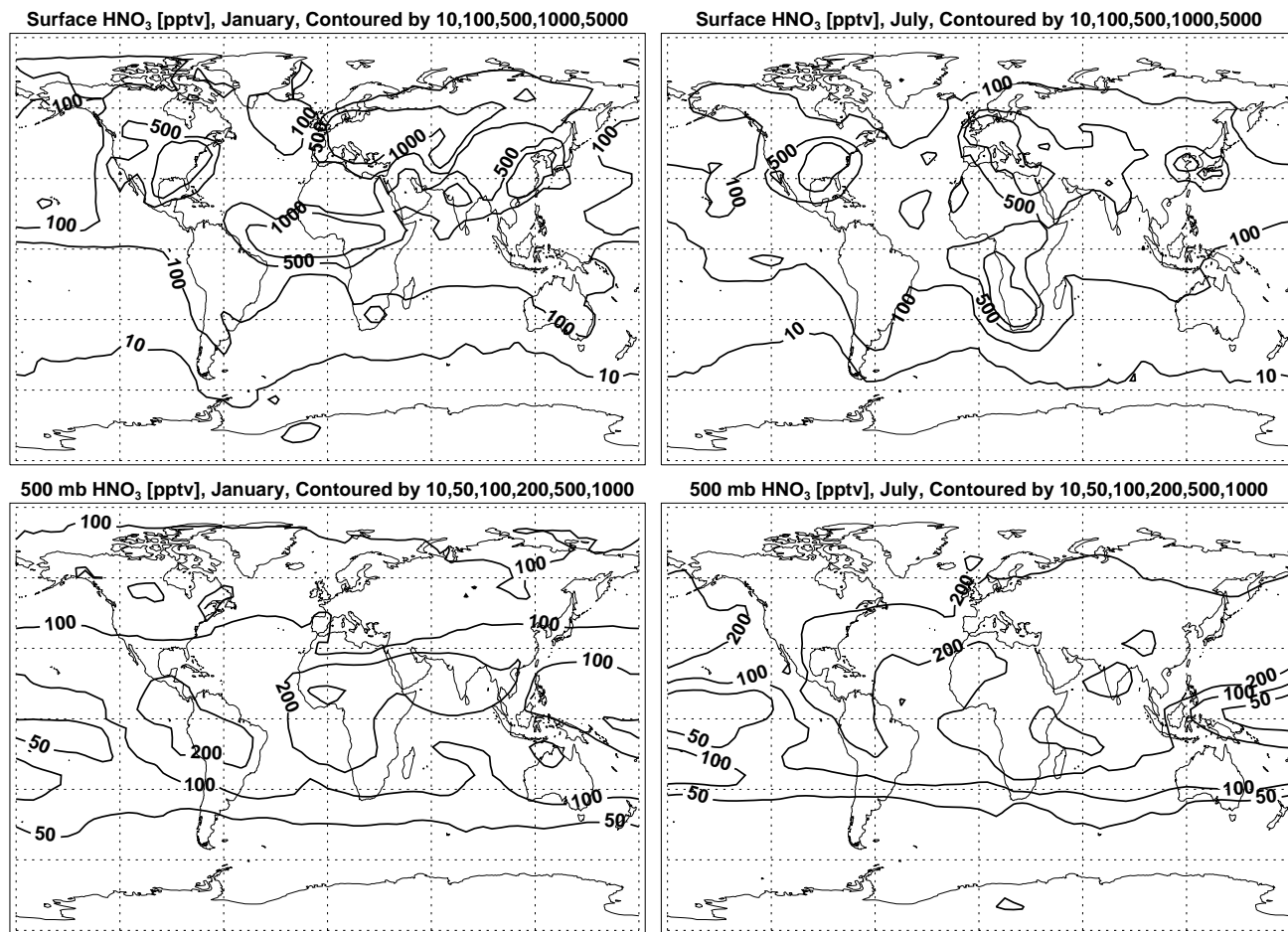


Fig. 6 (Bottom)

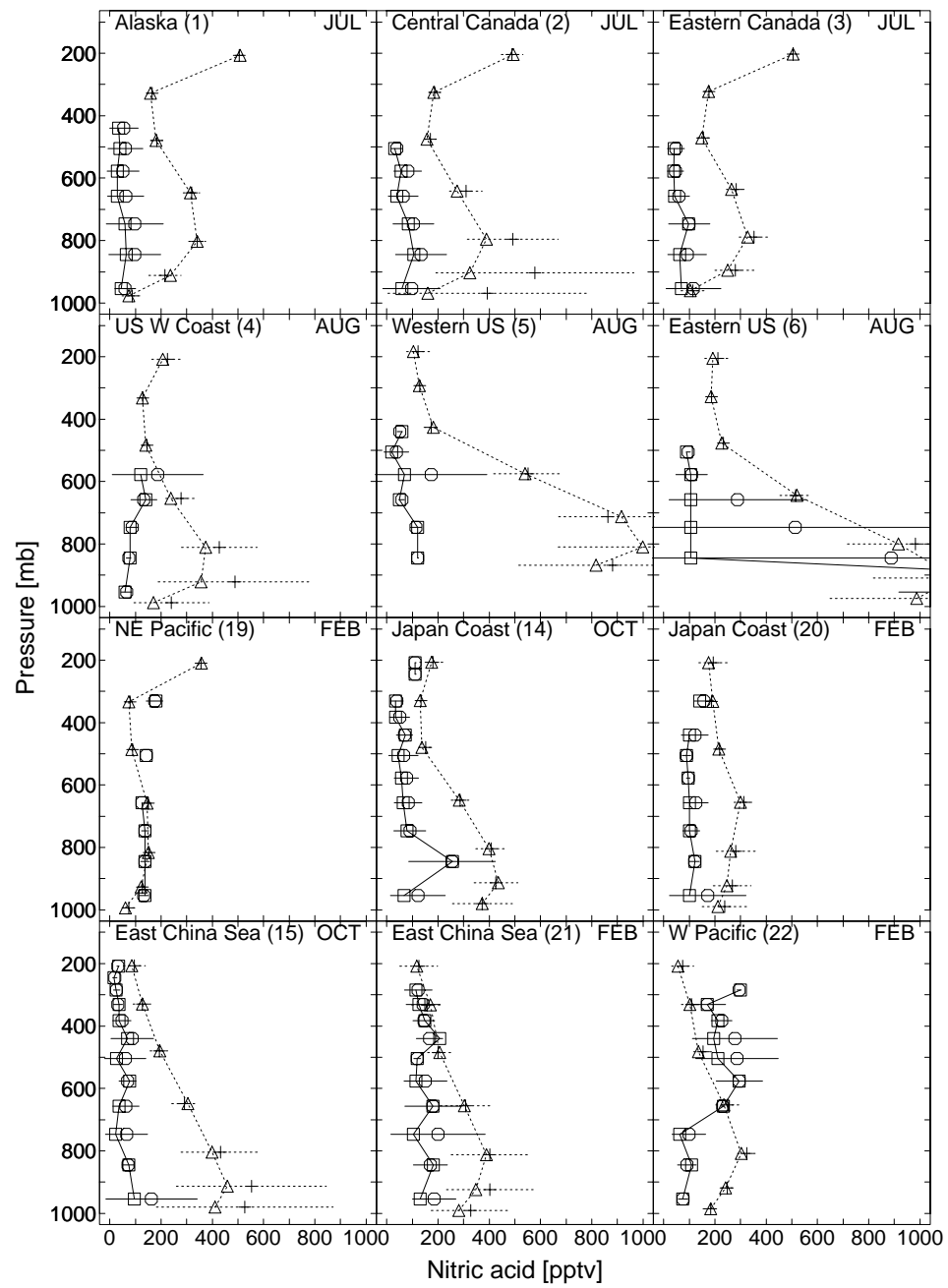


Fig. 7 (Bottom)

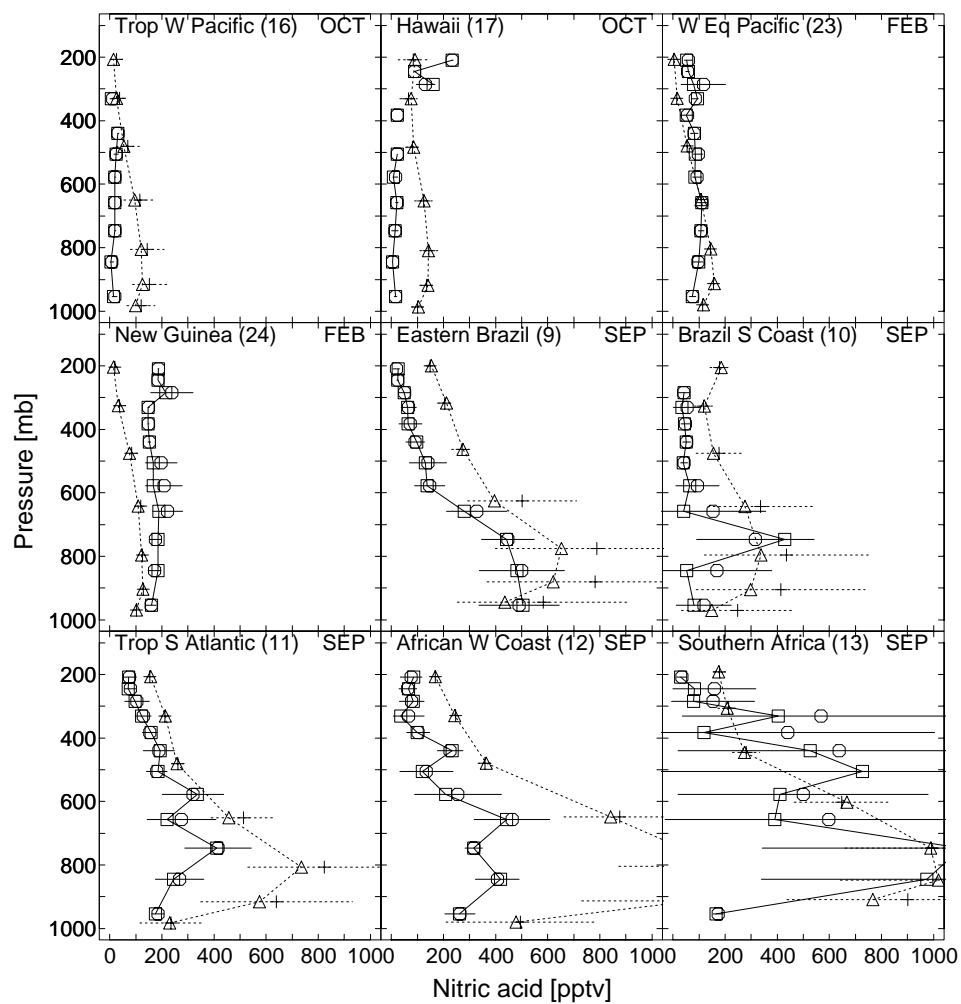


Fig. 7 (cont.) (Bottom)

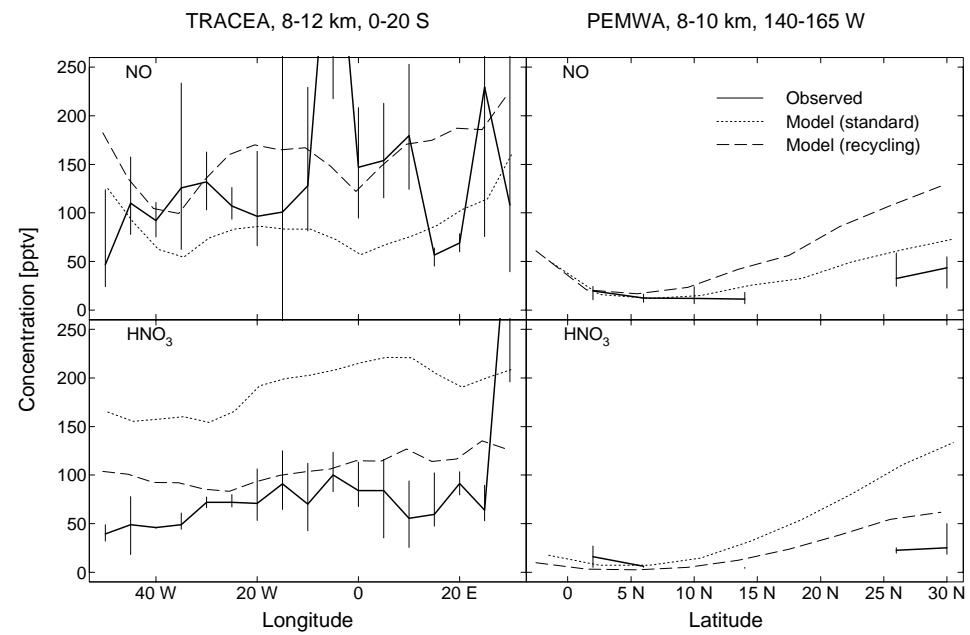


Fig. 8 (Bottom)

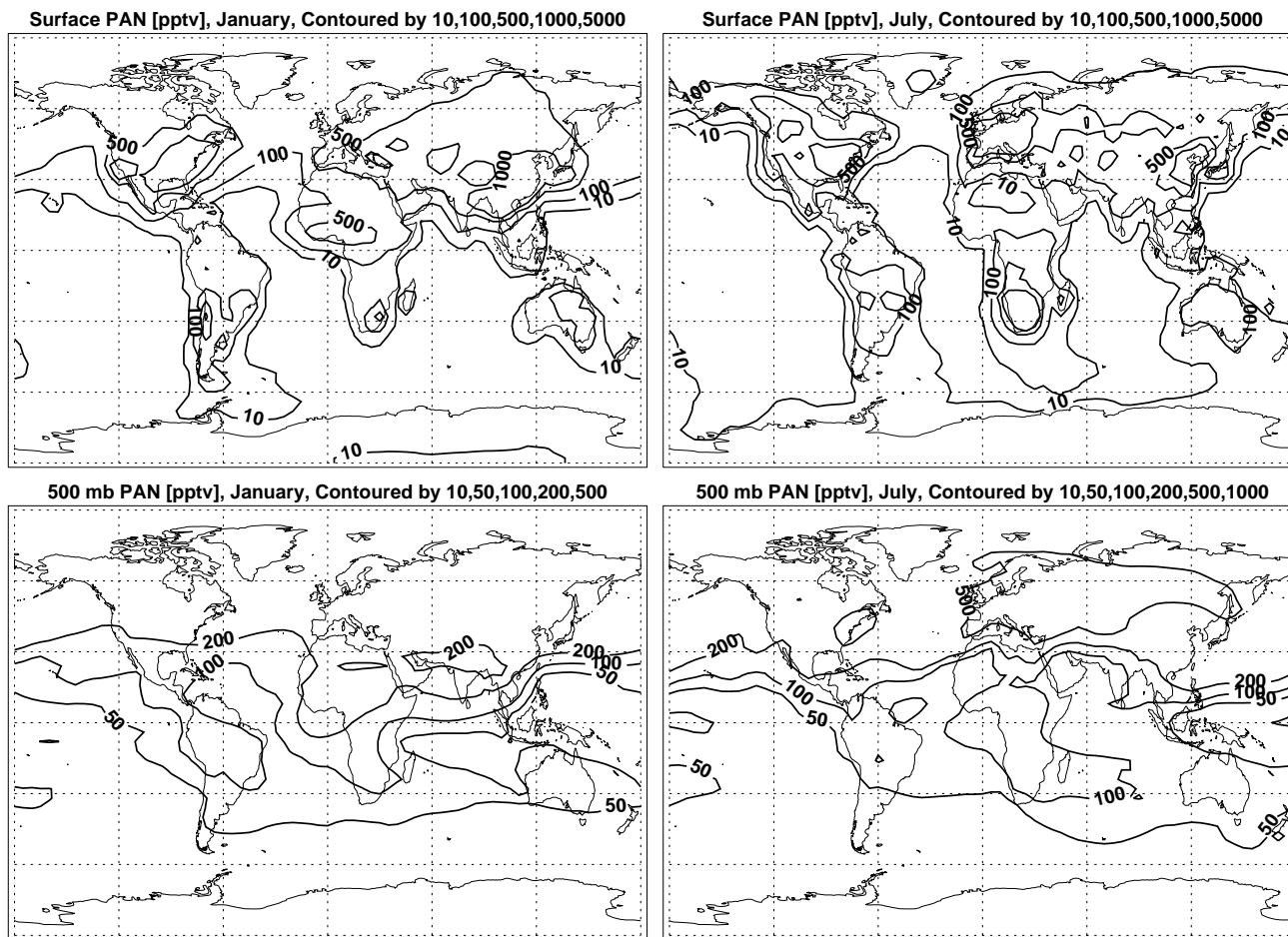


Fig. 9 (Bottom)

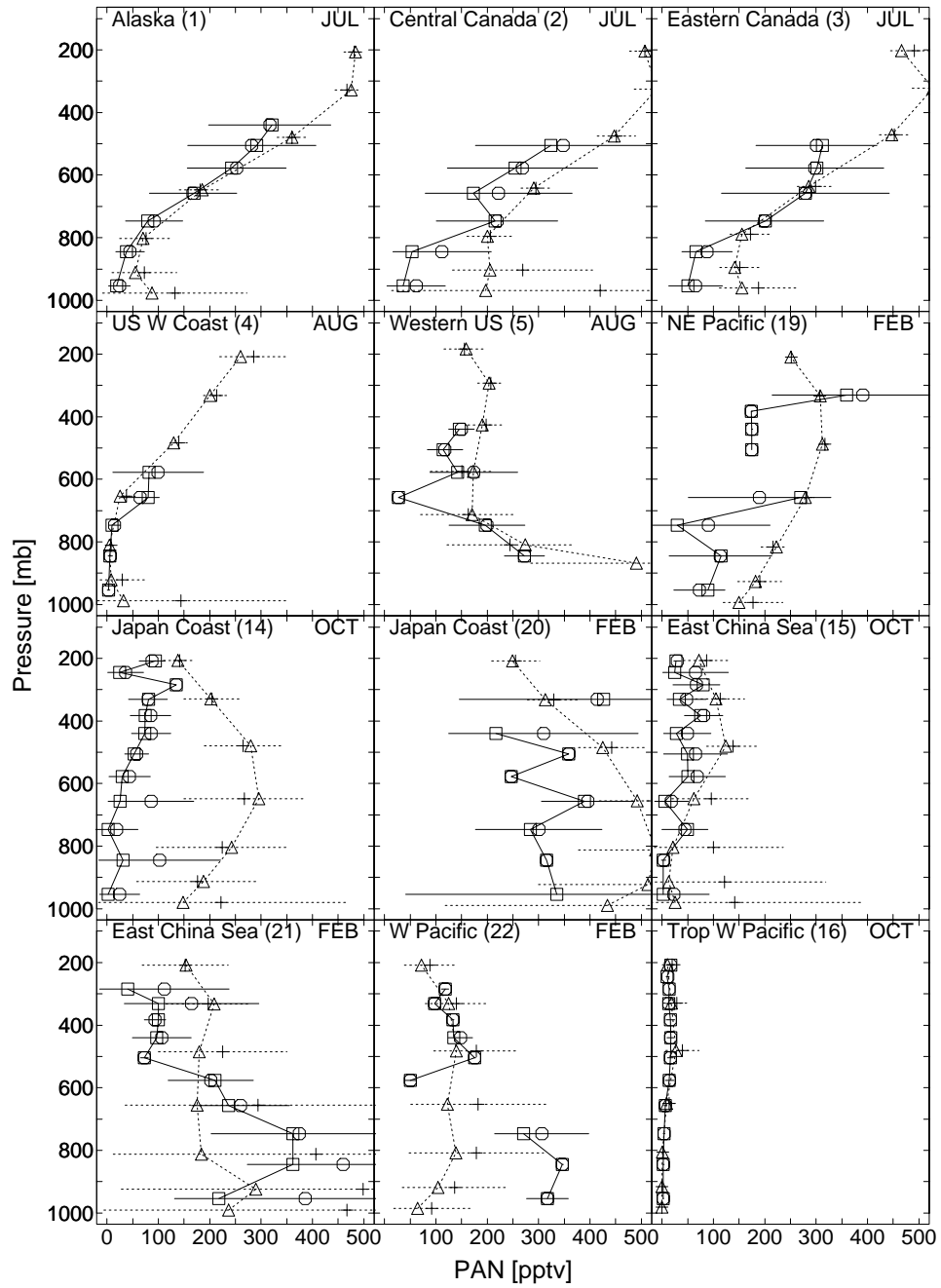


Fig. 10 (Bottom)

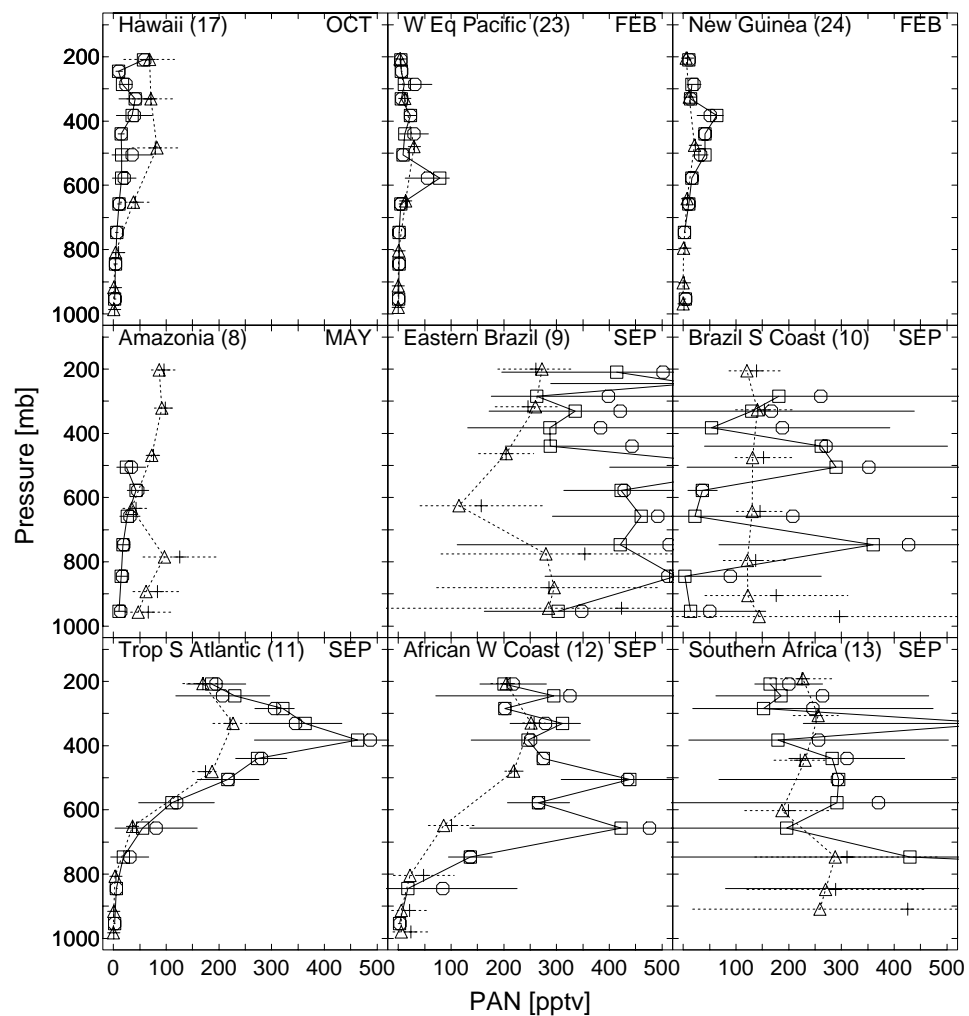


Fig. 10 (cont.) (Bottom)

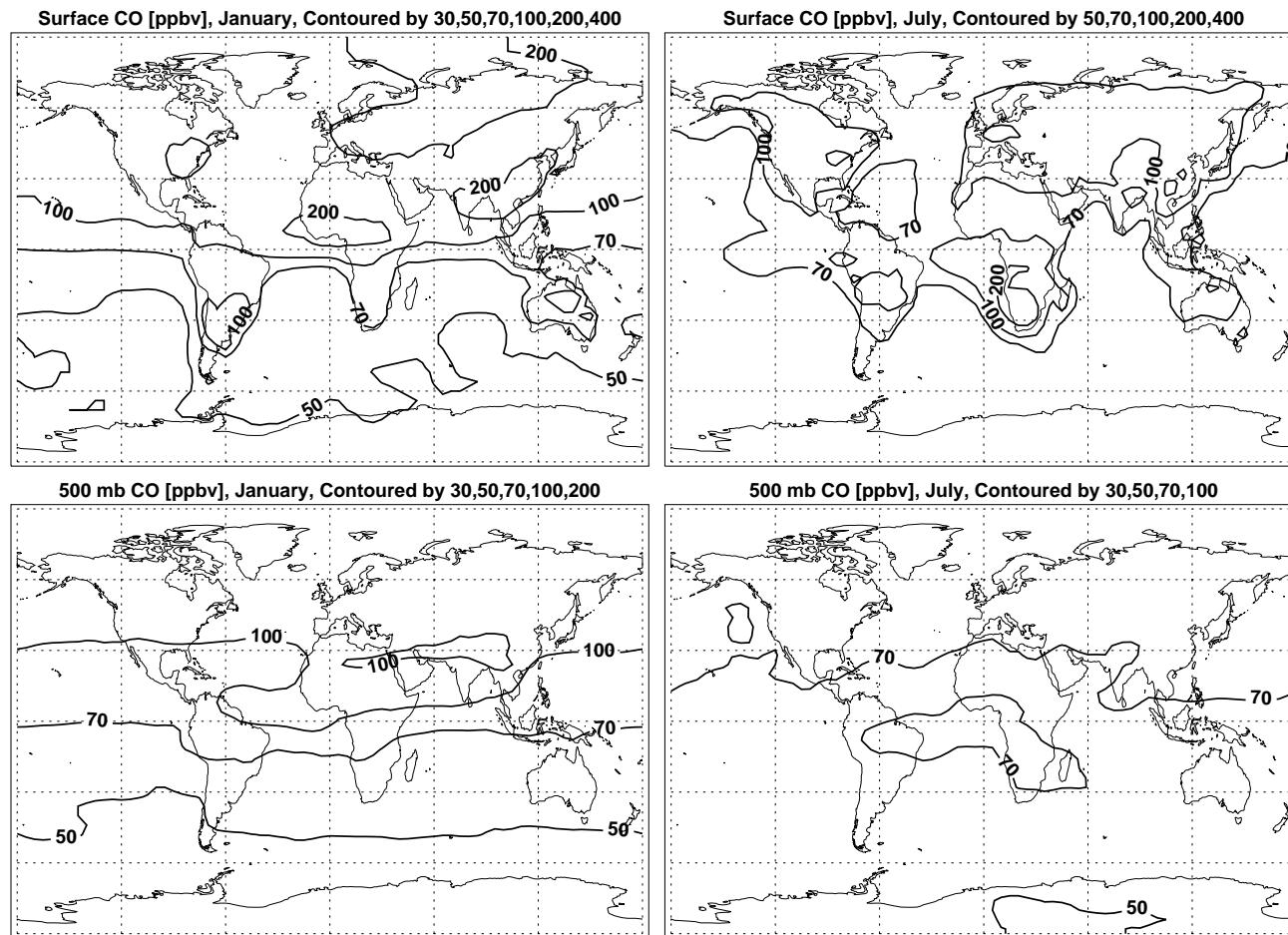


Fig.11 (Bottom)

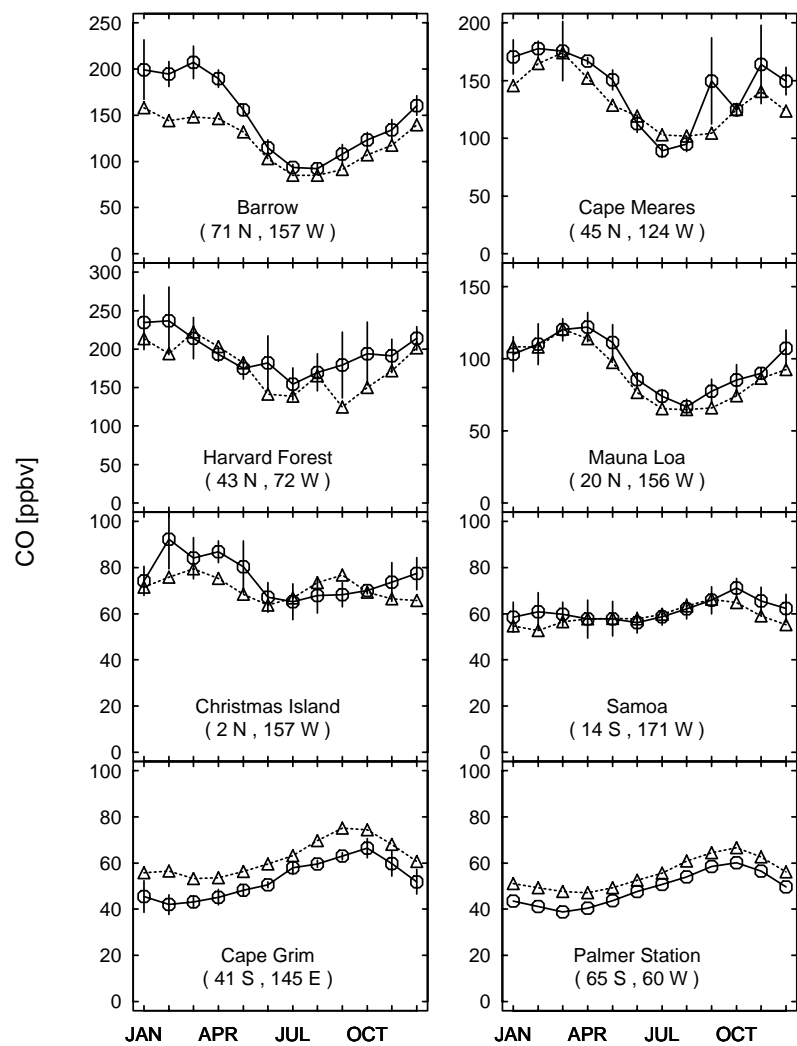


Fig. 12 (Bottom)

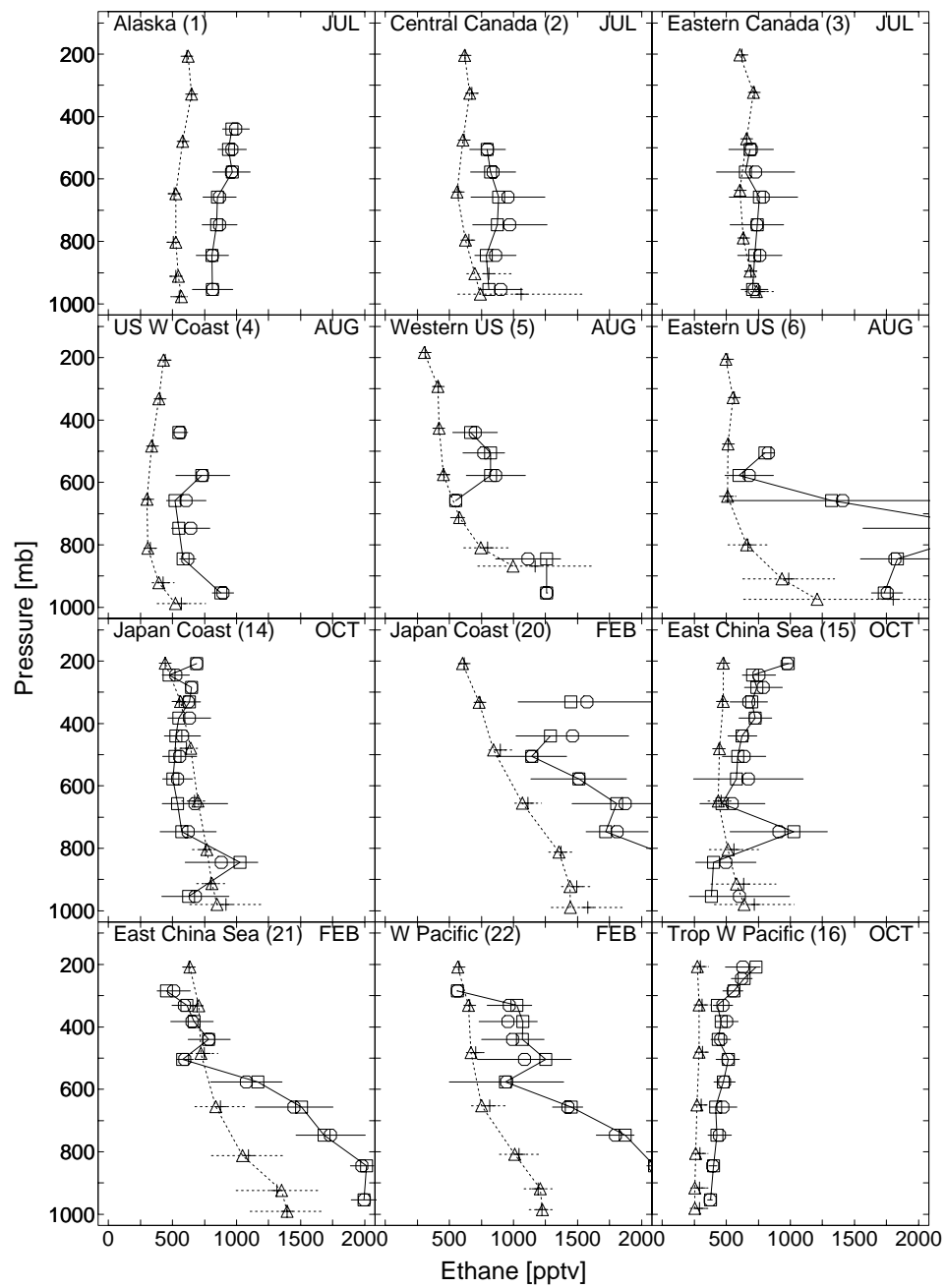


Fig. 13 (Bottom)

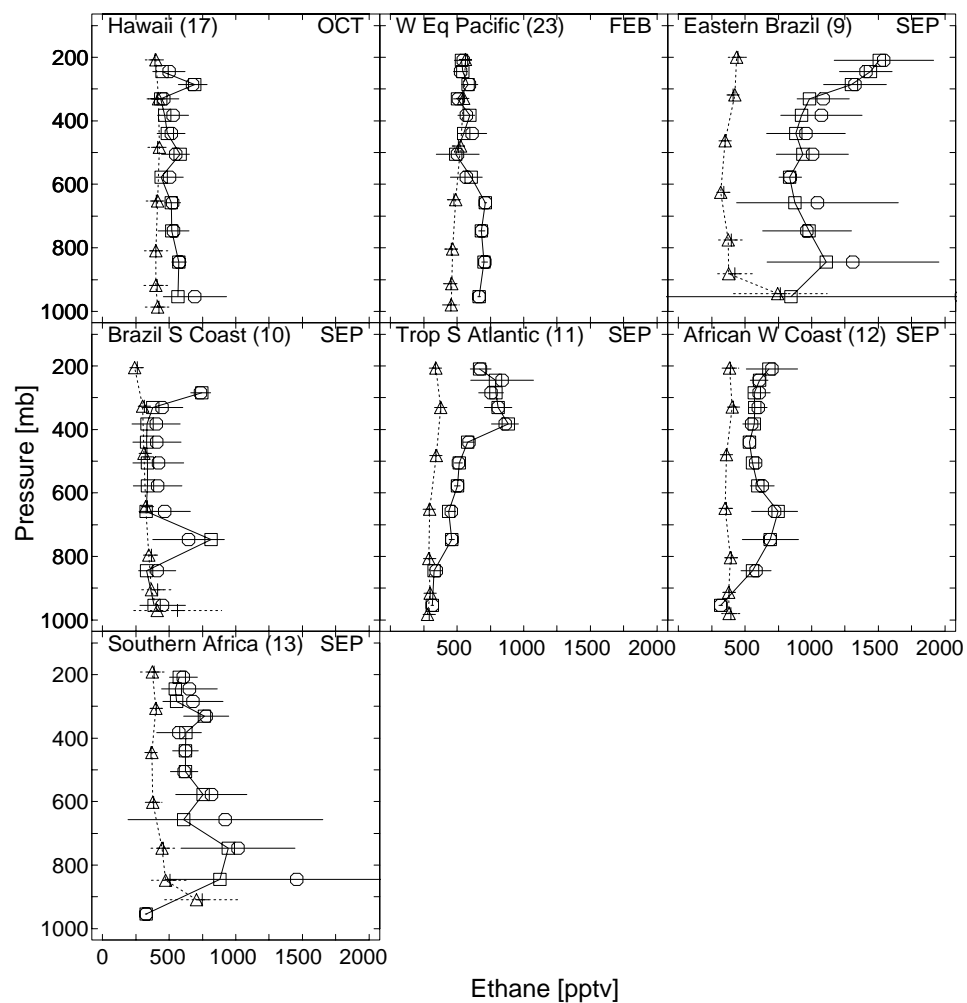


Fig. 13 (cont.) (Bottom)

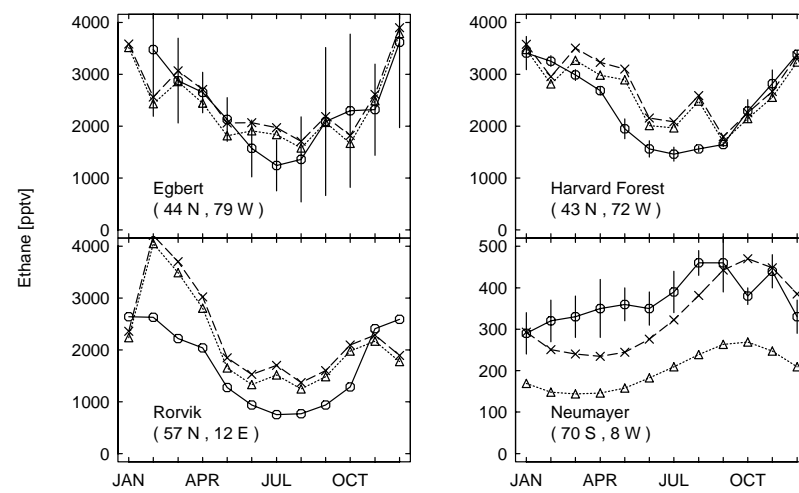


Fig. 14 (Bottom)

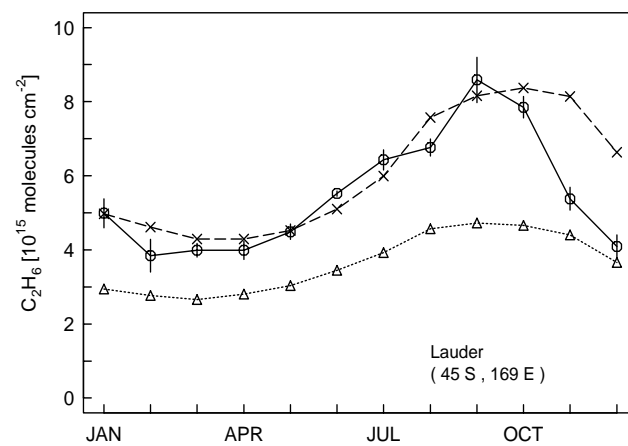
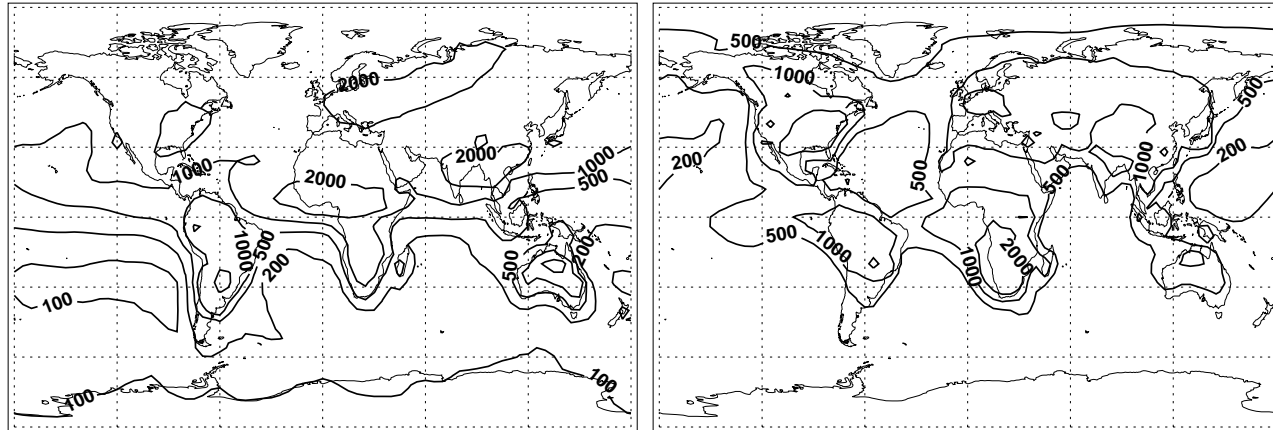


Fig. 15 (Bottom)

Surface Acetone [pptv], January, Contoured by 50,100,200,500,1000,2000 Surface Acetone [pptv], July, Contoured by 100,200,500,1000,2000



500 mb Acetone [pptv], January, Contoured by 10,50,100,200,500,1000,2000 500 mb Acetone [pptv], July, Contoured by 100,200,500,1000

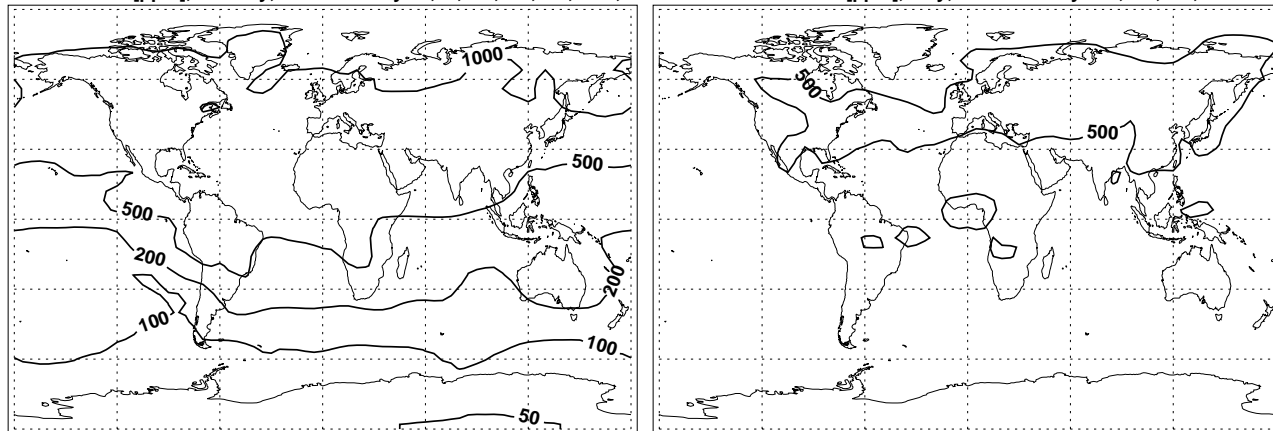


Fig.16 (Bottom)

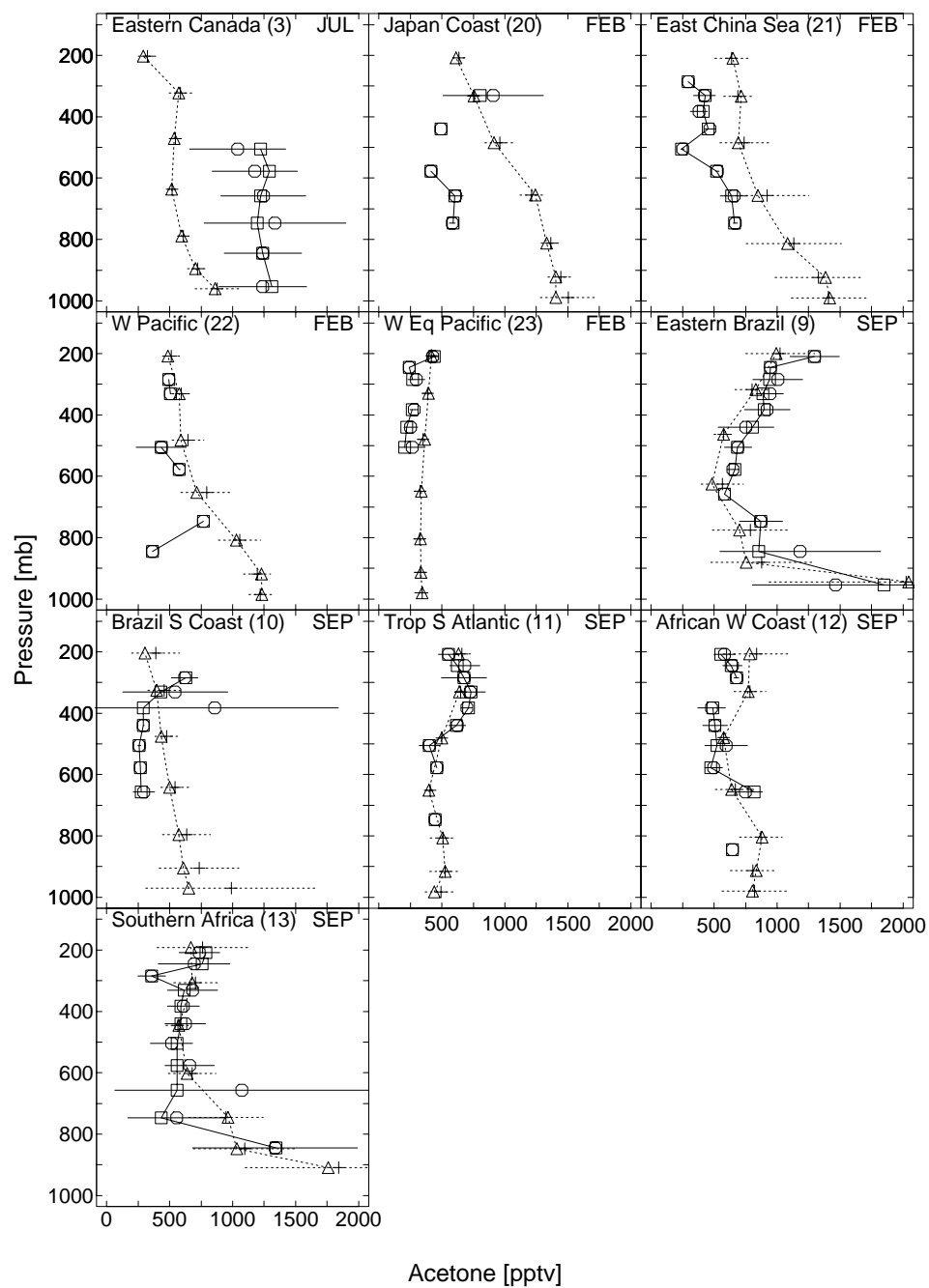


Fig. 17 (Bottom)

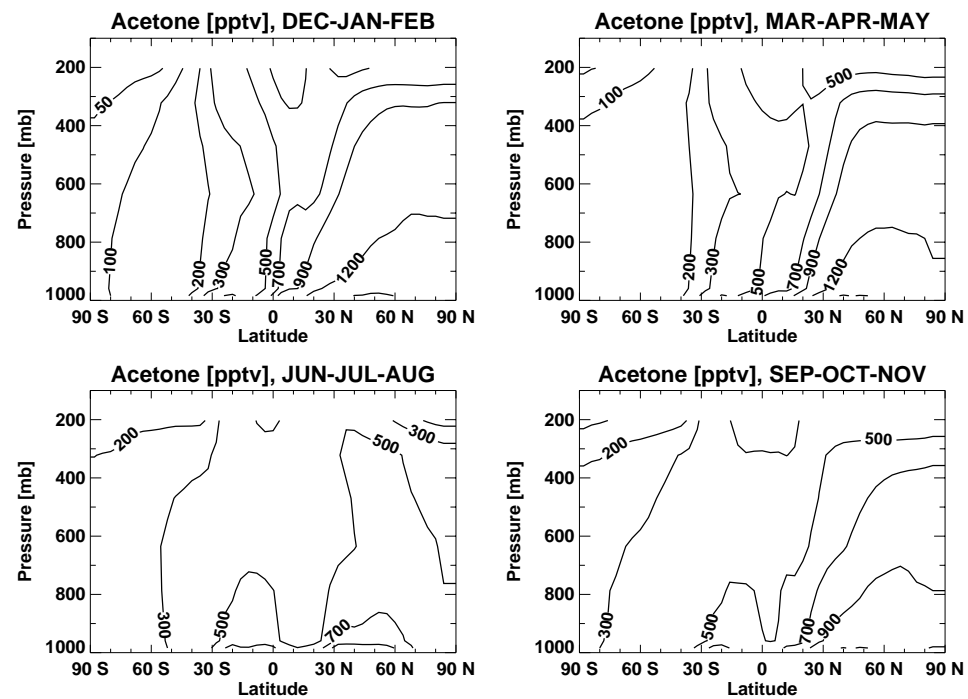
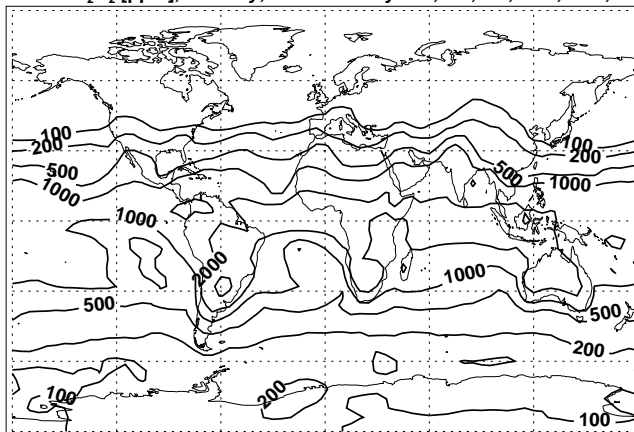
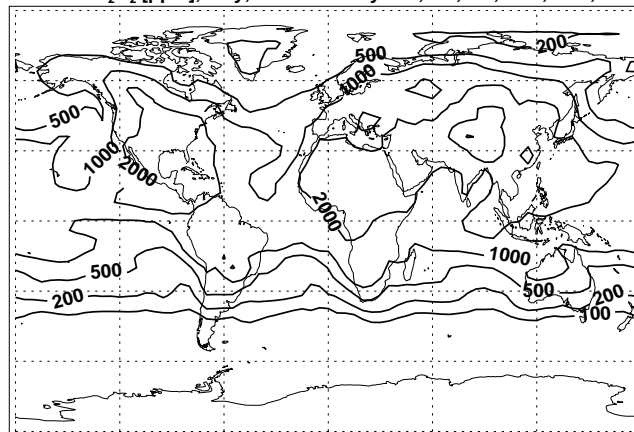


Fig. 18 (Bottom)

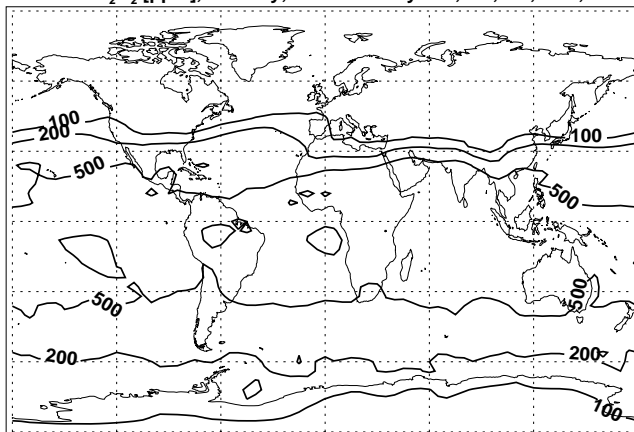
Surface H_2O_2 [pptv], January, Contoured by 100,200,500,1000,2000,5000



Surface H_2O_2 [pptv], July, Contoured by 100,200,500,1000,2000,5000



500 mb H_2O_2 [pptv], January, Contoured by 100,200,500,1000,2000



500 mb H_2O_2 [pptv], July, Contoured by 100,200,500,1000,2000

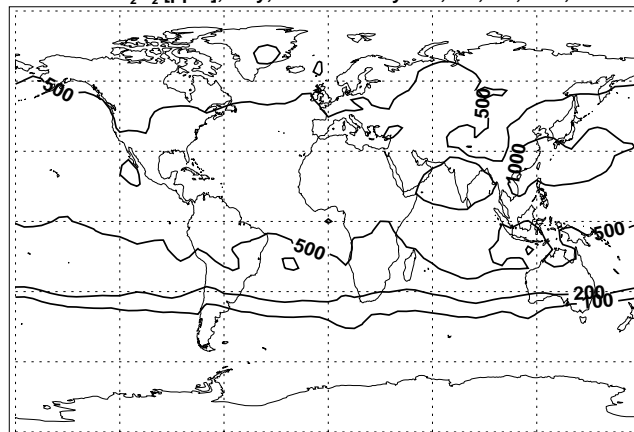


Fig. 19 (Bottom)

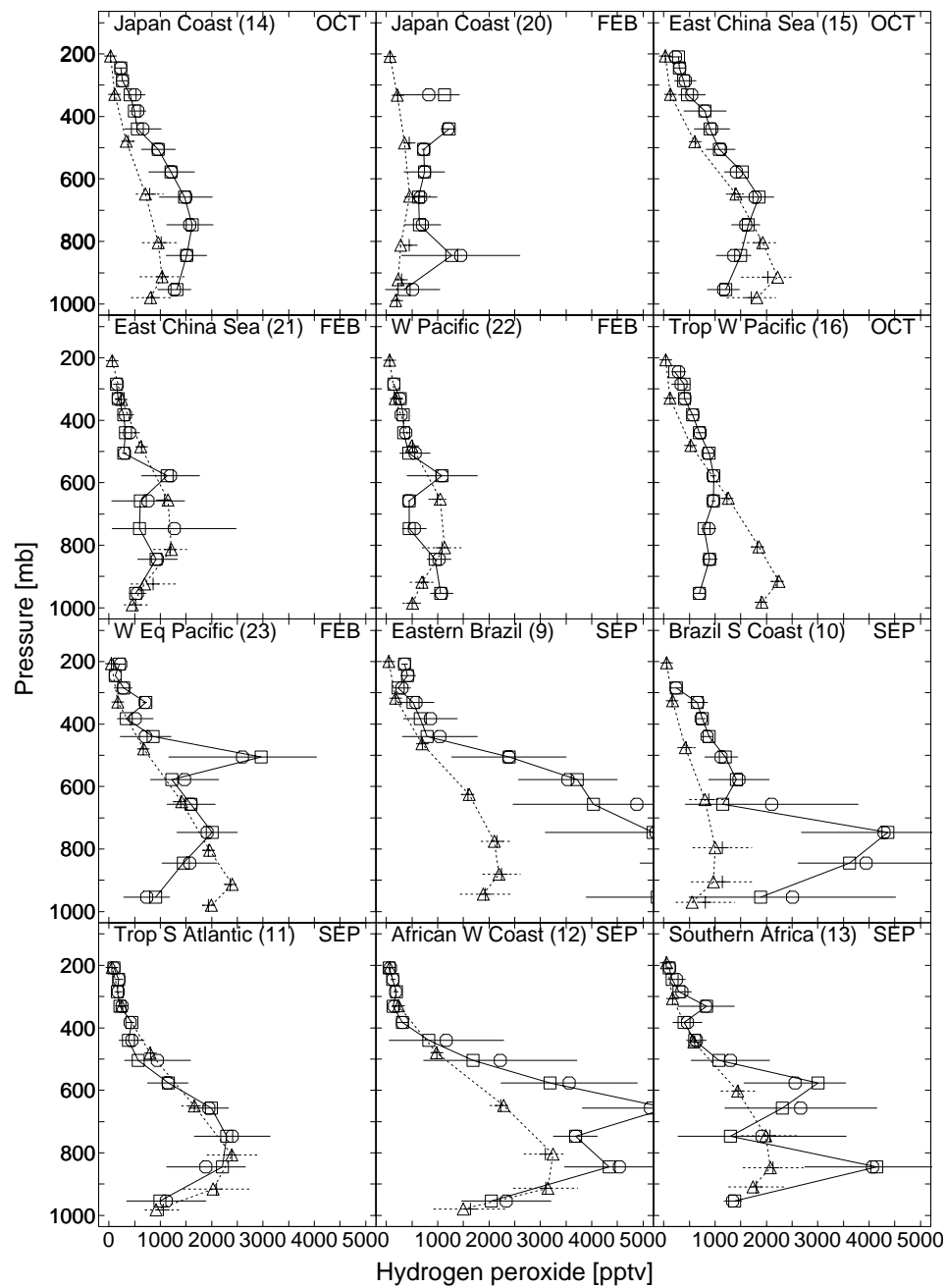


Fig. 20 (Bottom)

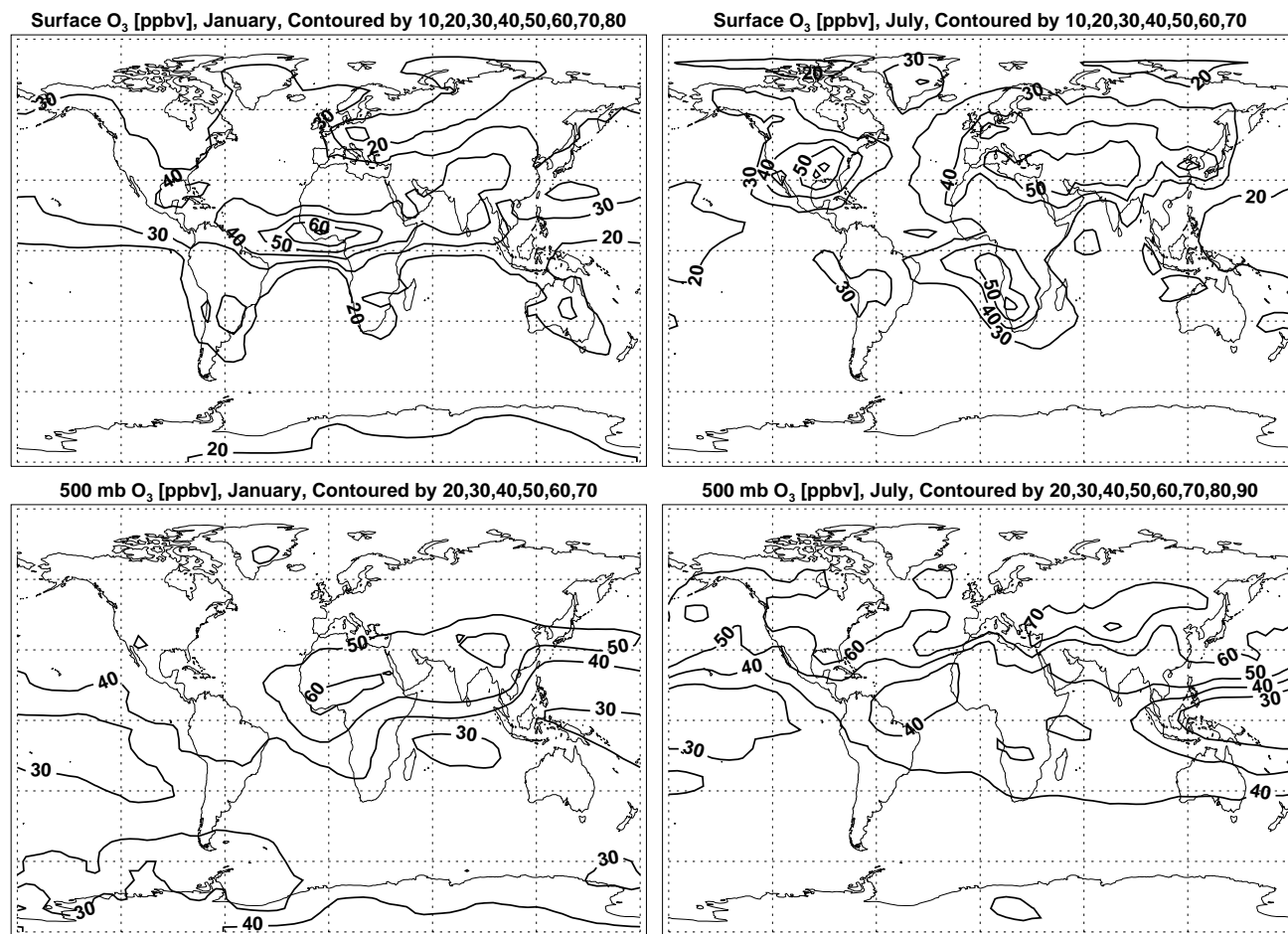


Fig. 21 (Bottom)

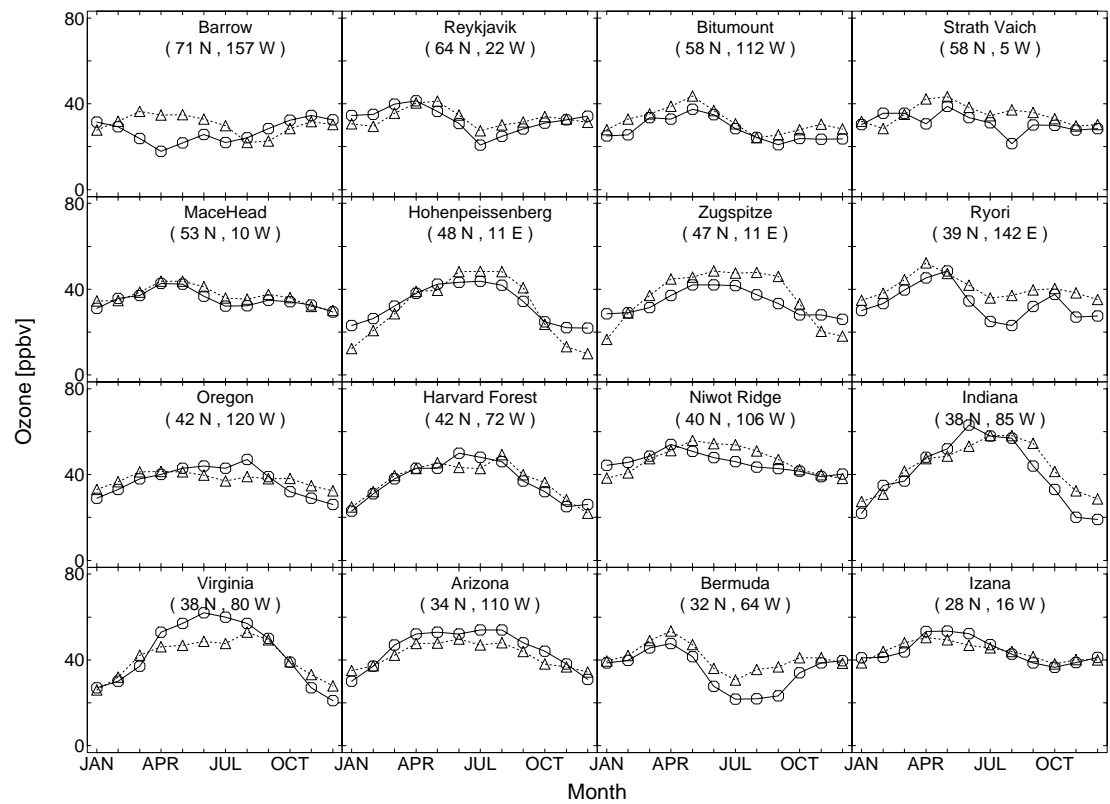


Fig. 22a (Bottom)

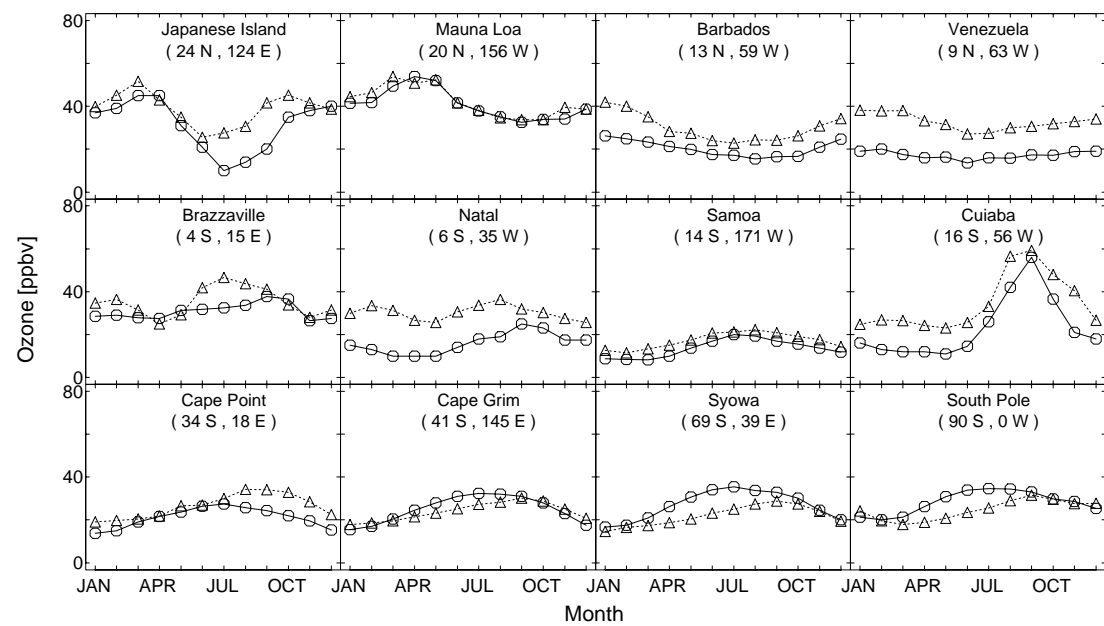


Fig. 22a (cont.) (Bottom)

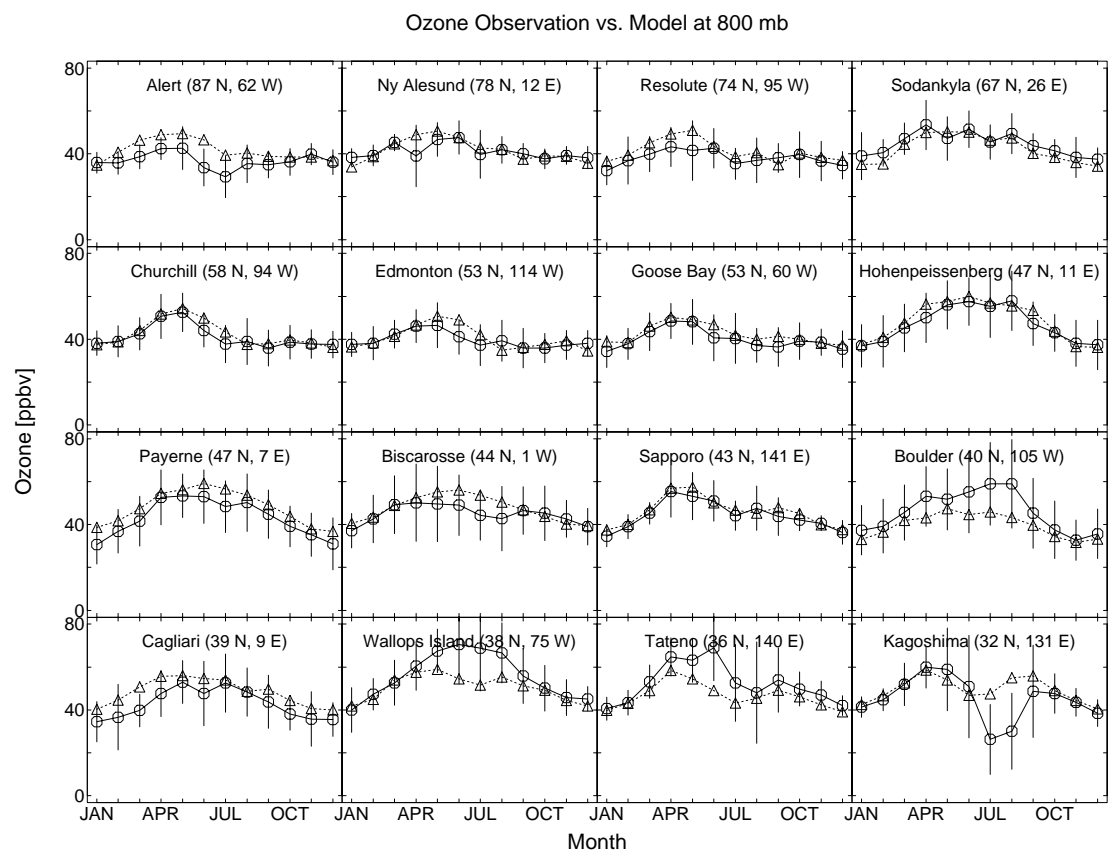


Fig. 22b (Bottom)

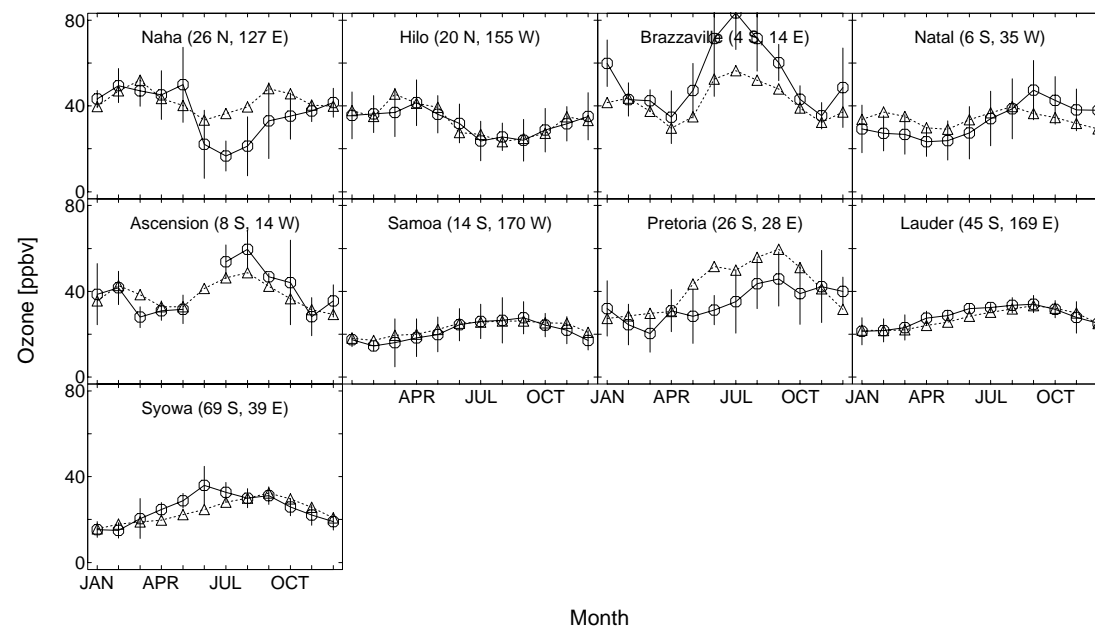


Fig. 22b (cont.) (Bottom)

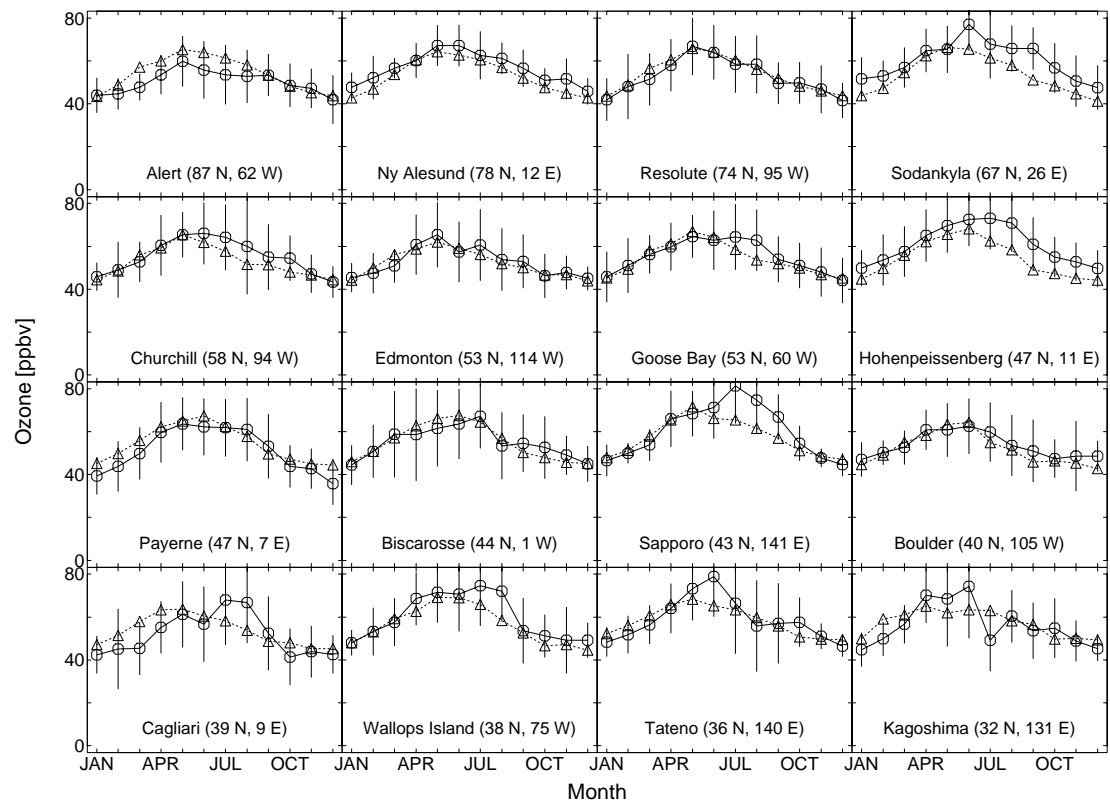


Fig. 22c (Bottom)

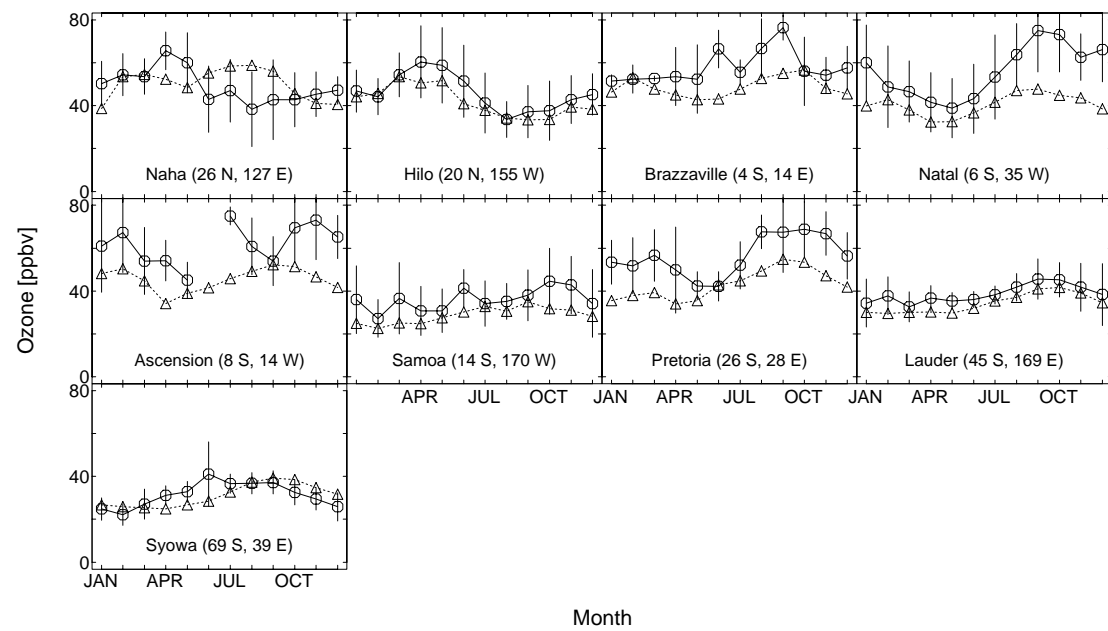


Fig. 22c (cont.) (Bottom)

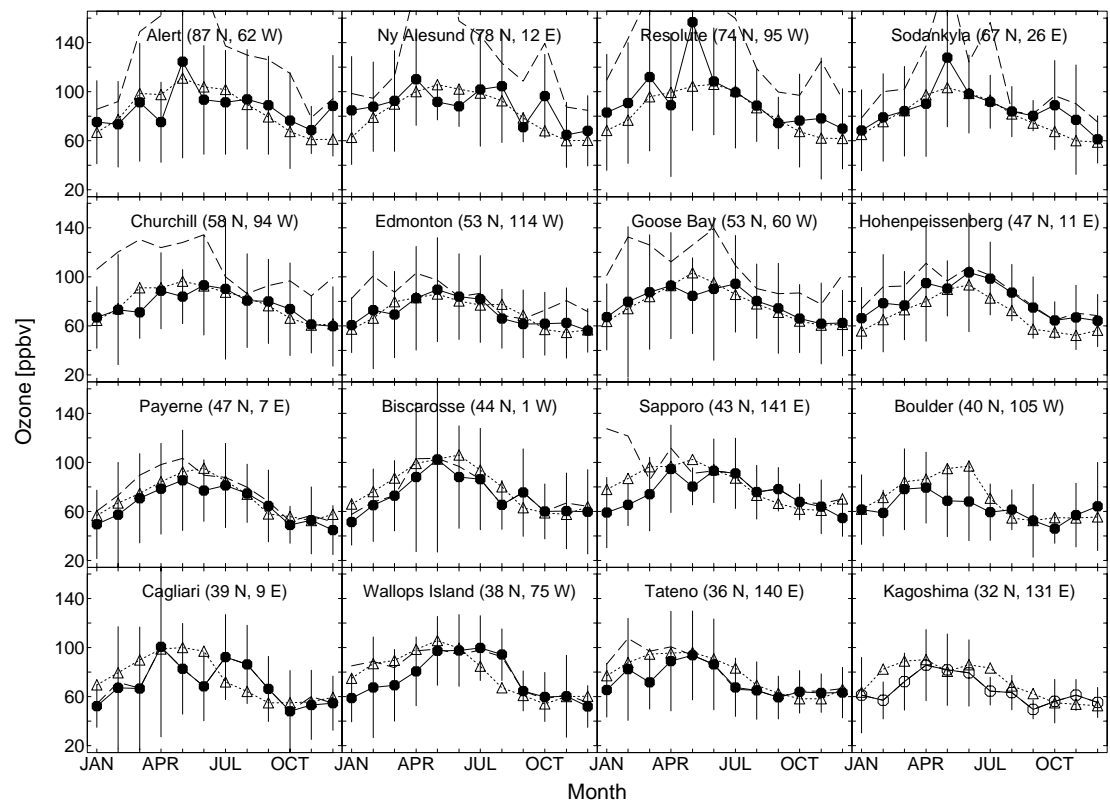


Fig. 22d (Bottom)

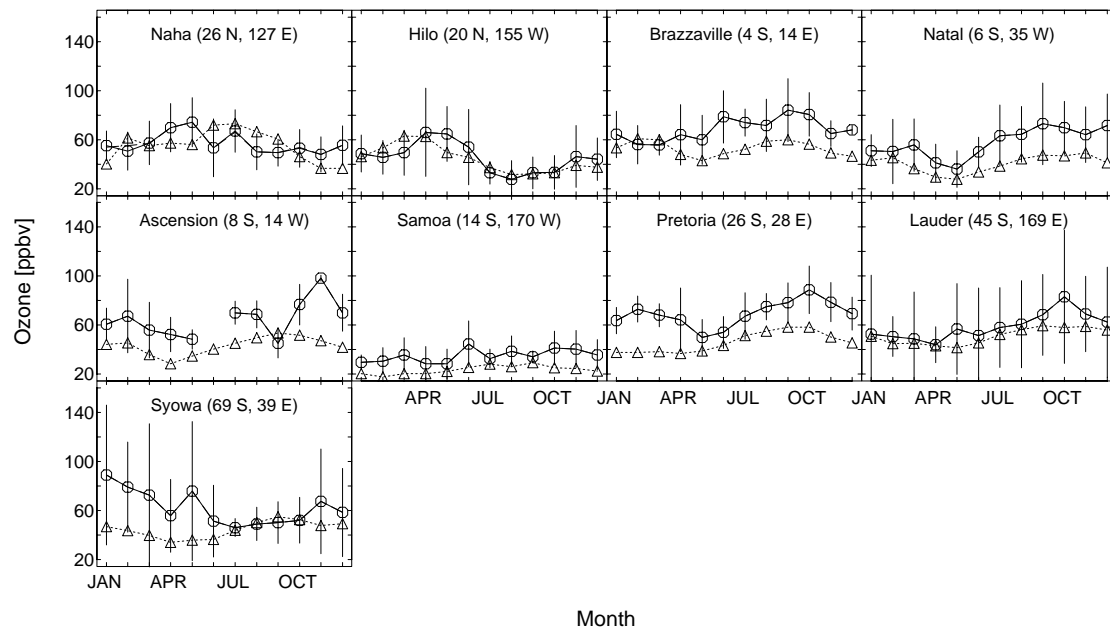


Fig. 22d (cont.) (Bottom)

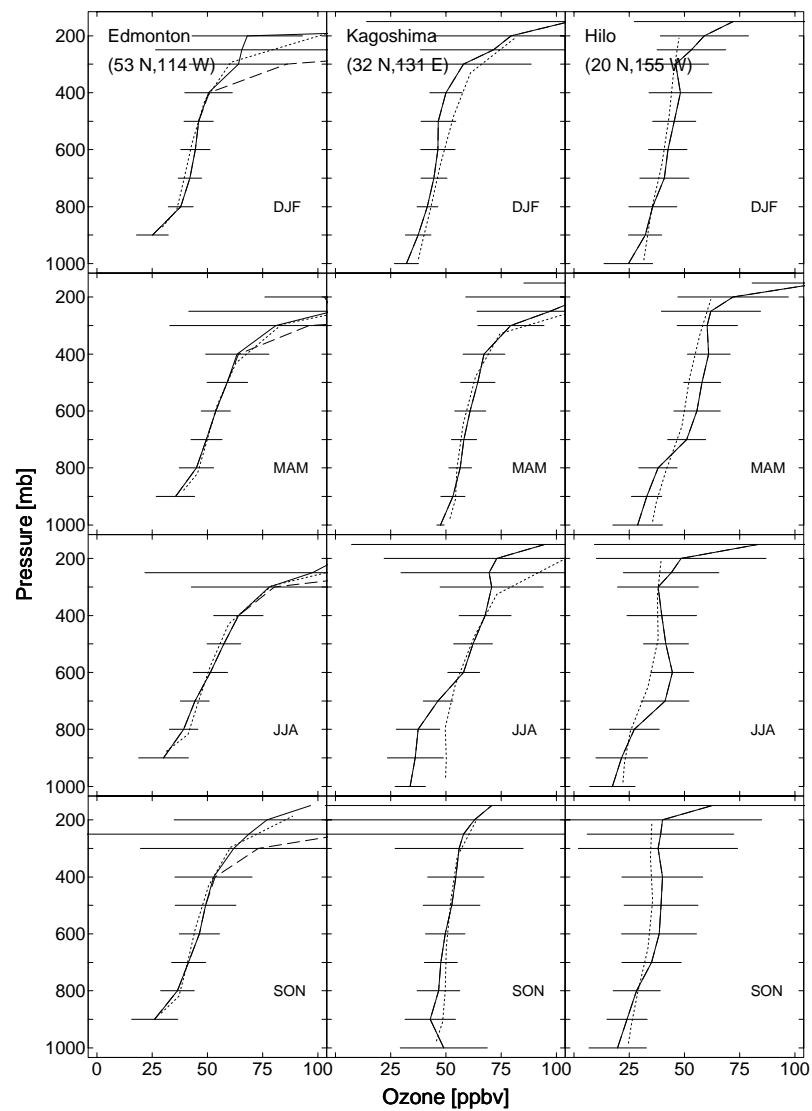


Fig. 23 (Bottom)

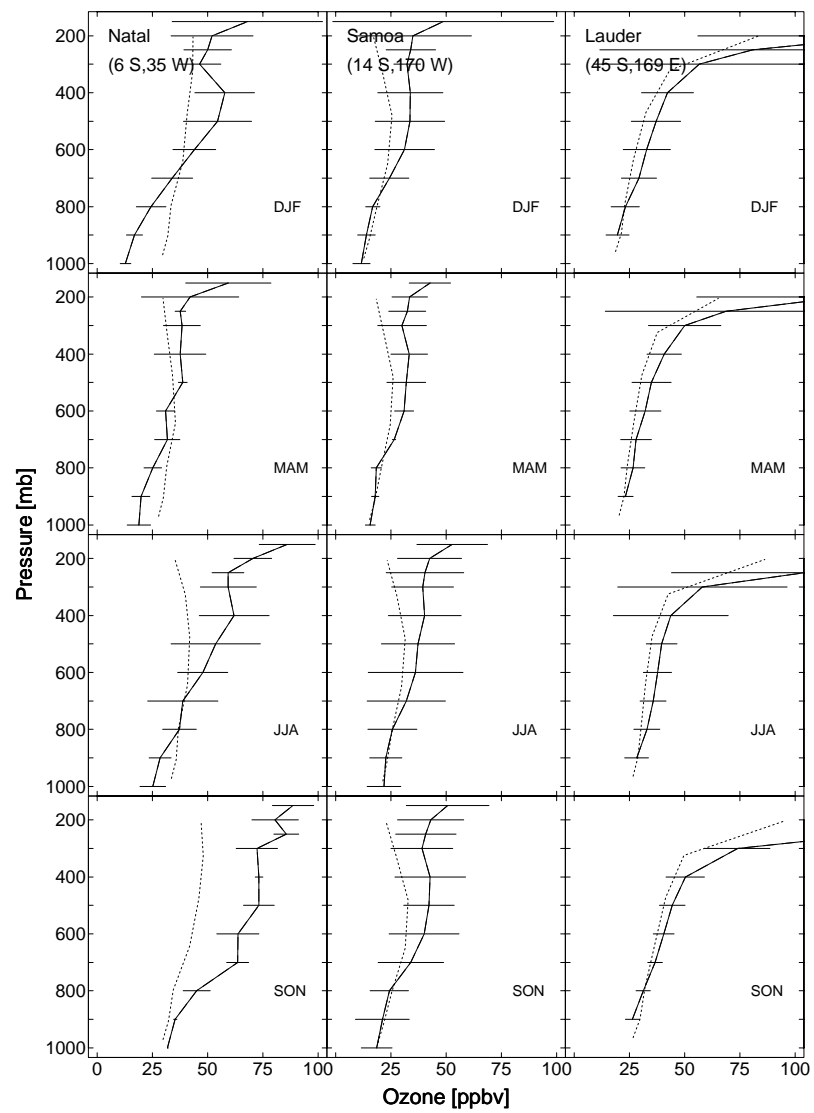


Fig. 23 (cont.) (Bottom)